Article:
Nischal, N, Oberheide, J, Mlynczak, MG et al. (2 more authors) (2019) Solar Cycle Variability of Nonmigrating Tides in the 5.3 and 15 μm Infrared Cooling of the Thermosphere (100–150 km) from SABER. Journal of Geophysical Research: Space Physics, 124 (3). pp. 2338-2356. ISSN 2169-9380

https://doi.org/10.1029/2018JA026356

Solar cycle variability of nonmigrating tides in the 5.3 μm and 15 μm infrared cooling of the thermosphere (100-180 km) from SABER

N. Nischal[1], J. Oberheide[1], M. G. Mlynczak[2], D. R. Marsh[3], Q. Gan[1]

[1]Department of Physics and Astronomy, Clemson University, Clemson, SC, USA
[2]NASA Langley Research Center, Hampton, VA, USA
[3]National Center for Atmospheric Research, Boulder, CO, USA

Key Points:

- Large solar cycle effect in 5.3 μm cooling rate tides due to temperature but increasing contribution from tidal advection during solar min
- 15 μm cooling rate tides more important during solar min but 5.3 μm tides more important during solar max above 120 km
- Tides in IR cooling rates suitable proxy for height evolution of tidal spectrum in thermosphere

Corresponding author: Nirmal Nischal, nnischa@g.clemson.edu

Abstract

This paper discusses the solar cycle variation of the DE3 and DE2 nonmigrating tides in the nitric oxide (NO) 5.3 μm and carbon dioxide (CO_2) 15 μm infrared cooling between 100 and 150 km altitude and +/-40 deg latitude. Tidal diagnostics of SABER NO and CO_2 cooling rate data (2002-2013) indicate DE3 (DE2) amplitudes during solar maximum are on the order of 1 (0.5) nW/m^3 in NO near 125 km, and on the order of 60 (30) nW/m^3 in CO_2 at 100 km, which translates into roughly 15-30% relative to the monthly zonal mean. The NO cooling shows a pronounced (factor of 10) solar cycle dependence (lower during solar minimum) while the CO_2 cooling does not vary much from solar min to solar max. Photochemical modeling reproduces the observed solar cycle variability and allows one to delineate the physical reasons for the observed solar flux dependence of the tides in the infrared cooling, particularly in terms of warmer/colder background temperature versus smaller/larger tidal temperatures during solar max/min, in addition to cooling rate variations due to vertical tidal advection and tidal density variations. Our results suggest that (i) tides caused by tropospheric weather impose a substantial - and in the NO 5.3 μm case solar cycle dependent- modulation of the infrared cooling, mainly due to tidal temperature (ii) observed tides in the infrared cooling are a suitable proxy for tidal activity including its solar cycle dependence in a part of Earth$'$s atmosphere where direct global temperature observations are lacking.

1 Introduction

Atmospheric tides play an important role in coupling the lower and upper atmosphere via transport of energy and momentum. These tides originate close to the Earth's surface, either as a result of latent heat release in the deep convective clouds, or through periodic absorption of solar radiation by tropospheric water vapor and stratospheric ozone. In addition, they can also be generated from wave-wave interactions. The accepted convention to refer to a tide is to denote its period (D for diurnal, S for semidiurnal, and so on), propagation direction (E for eastward propagating and W for westward propagating) and zonal wave number, such that, DE3 is for diurnal eastward propagating tide with zonal wave number 3. Tides can propagate upward and introduce significant variability in the middle and upper atmosphere by modulating temperature [*Zhang et al.*, 2006; *Forbes et al.*, 2008; *Akmaev et al.*, 2008], winds [*Lühr et al.*, 2007; *Hagan et al.*, 2009; *Talaat and Lieberman*, 2010; *Häusler et al.*, 2013], compositional structures [*Oberheide and Forbes*, 2008; *Zhang et al.*, 2010; *England et al.*, 2010], and plasma and neutral densities [*Oberheide et al.*, 2009; *Chang et al.*, 2013]. These studies along with several others [e.g *Häusler et al.*, 2007; *Häusler and Lühr*, 2009; *Forbes et al.*, 2009; *Häusler et al.*, 2010] have shown that the impact of tropospheric tides can be observed in the upper thermosphere, including the ionospheric dynamo region. Various observations and modeling studies [*Sagawa et al.*, 2005; *Immel et al.*, 2006; *Hagan et al.*, 2007; *Lühr et al.*, 2008] have shown that the presence of wave-4 structures in the low latitude F-region ionospheric parameters can be attributed to the modulation by atmospheric tides, particularly by the DE3, thereby confirming the importance of the role these waves play in transmitting global-scale tropospheric weather signals to the middle and upper atmosphere.

All these studies suggest that similar effects can be expected in various other parameters important to the physics of the Ionosphere-Thermosphere (IT) system such as the energy budget of the thermosphere and its infrared (IR) cooling. Relatively less work has been directed towards understanding the impact of atmospheric tides, especially of those originating near the Earth's surface, on the thermospheric emissions responsible for its cooling. NO at 5.3 μm [*Kockarts*, 1980] and CO_2 at 15 μm [*Curtis and Goody*, 1956] IR emissions are the major cooling mechanisms that contribute to the energy budget of the thermosphere in the altitude range of 100-200 km. NO emissions, in particular, acts as the Earth's upper atmosphere's natural thermostat [*Mlynczak et al.*, 2003], and make major

contributions towards the energy balance of the thermosphere. Furthermore, tidal observations in temperature and winds in the thermosphere are sparse. As such, studies aimed at exploring the impacts of atmospheric tides on the thermospheric IR emissions will give an insight into the tidal dynamics of this region, particularly from observational point of view. Recent studies [*Oberheide et al.*, 2013; *Nischal et al.*, 2017] have shown that NO and CO_2 emissions in the thermosphere are significantly modulated in longitude/local time by the upward propagating nonmigrating tides, the DE2 and DE3. In addition, temperature has been found to be the main tidal driver of the NO and CO_2 cooling rate tides. These studies have been useful in understanding the response of the lower thermosphere to the atmospheric tides (both upward propagating and in-situ tides) as the upper boundary of SABER temperature observation is limited to 110 km and in-situ tidal diagnostics are only available either at 250 km (GOCE) or 400 km (CHAMP). A such, tides in NO and CO_2 cooling rates give new information about the height evolution of the tidal spectrum in the thermosphere.

Previous studies *Oberheide et al.* [2013]; *Nischal et al.* [2017], however, were focused for the solar minimum year 2008 and hence discussed the seasonal variation of observed cooling rate tides in the NO and CO_2 emissions. This paper now focuses on investigating the impact of solar cycle on the NO and CO_2 cooling rate tides. The motivation for the current work arises from the results reported by earlier studies which recognize temperature, neutral density and advection as the main tidal drivers of the observed nonmigrating tidal signals in NO and CO_2 infrared emissions. Solar cycle variation in temperature, density, horizontal and vertical winds have been reported by *Oberheide et al.* [2009], as such, one would expect similar effects in the cooling rate tides. Furthermore, tidally induced modulation in the mean temperature and thermospheric composition (O and therefore NO) has also been found by *Jones et al.* [2016]. Thermospheric NO variablity can also be attributed to the tropospheric nonmigrating tides [*Oberheide and Forbes*, 2008]. *Flynn et al.* [2018] discusses the seasonal and annual variability of NO flux over 14 years and highlights the contribution from diurnal tides. *Siskind et al.* [2019] has reported sources for the abundance and diurnal variation in NO at solar minimum consitions by simulating the mesospheric zonal winds. Moreover, *Mlynczak et al.* [2010] showed that both NO and CO_2 radiative cooling in the thermosphere have a strong solar cycle dependence. Hence, the current work aims to study solar cycle dependence of the observed nonmigrating tidal signals in the NO and CO_2 cooling rates and highlights the possible sources of such effects. The dependence of relative contributions from the leading tidal drivers on the solar cycle is also investigated. As such, findings from this work can be used as a proxy for the solar cycle variation in the dynamical tides (tides in temperature, wind fields, etc.), especially the temperature, throughout the lower thermosphere region. The present study is limited to studying the effects of DE2 and DE3 nonmigrating tidal components because the overarching goal is to understand the impact of tropospheric weather on the energy loss rates in the lower thermosphere. Both the DE2 and DE3 nonmigrating tides that begin near the surface as heat is released by evaporation and condensation are well known to play a major role in modulating the middle and upper atmosphere dynamics [e.g *England*, 2012] and references therein. The importance of other nonmigrating tidal components and tides from other sources for the thermospheric energy budget will be investigated in the near future.

We employ SABER version 2.0 NO and CO_2 cooling rate data [*Mlynczak et al.*, 2010], dynamical tides from the CTMT empirical model [*Oberheide et al.*, 2011a,b] and photochemical modeling to answer the following two questions: (i) What are the longitudinal and local time variations in NO and CO_2 cooling rates caused by the DE2 and DE3 nonmigrating tides and what temporal variability (seasonal, inter-annual and solar cycle) do they exhibit? (ii) What are the leading coupling mechanisms and how do they respond at various time scales?

The paper is organized as follows: Section 2 provides an overview of the tidal diagnostics of SABER NO and CO_2 cooling rate data and presents the results of the data analysis. Section 3 shows the details of the empirical tidal and photochemical modeling. Section 4 contains the discussion and section 5 summarizes the findings of this work.

2 Tidal Diagnostics of SABER NO 5.3 μm and CO_2 15 μm Cooling Rates

2.1 Data and Methodology

The SABER instrument [*Russell et al.*, 1999] aboard NASA TIMED satellite is a 10 channel limb scanning radiometer that has been providing continuous data coverage since early 2002. SABER views the atmosphere 90° to the satellite velocity vector and measures infrared radiance ($Wm^{-2}sr^{-1}$) every 0.4 km in a 625 km, 74° inclination orbit. The latitude coverage on any particular day is between 53°S and 83°N in the northward looking mode and between 83°S and 53°N during the southward looking mode. A 180° yaw maneuver is performed every 60 days to keep the spacecraft away from the Sun. This results in an alternate viewing geometry of SABER every 60 days. As a result of local time precession of the TIMED satellite, it takes 60 days to provide a full 24 hr local time coverage. About 15 longitudes are sampled every day on the ascending and descending nodes of the orbit. An infrared radiance height profile is sampled every 53 s. For our current analysis we employ version 2.0 SABER NO 5.3 μm and CO_2 15 μm emission data. NO emission is observed up to 300 km whereas CO_2 emissions are measured up to 139 km and a detailed explanation of the derivation of the infrared radiative cooling rates (Wm^{-3}) for NO and CO_2 emissions can be found in *Mlynczak et al.* [2010]. The accuracy of NO and CO_2 cooling rates is 15% and hence so are the tidal amplitudes from the current tidal analysis.

The DE2 and DE3 amplitudes and phases in NO 5.3 μm and CO_2 15 μm cooling rates are computed using methods described in *Oberheide et al.* [2013] and *Nischal et al.* [2017], respectively. The approach employed in these mentioned papers is a very frequently used method of deriving tidal amplitudes and phases from satellite data and has been employed in several tidal studies [*Forbes and Wu*, 2006; *Forbes et al.*, 2008]. For NO tidal diagnostic, all 5.3 μm volume emission rate (VER) data collected within a 2 day window following a 3-hourly Kp $\geq$ 4 event are omitted from the analysis. Nevertheless, this omission still leaves > 40 days (in most cases > 50 days) within a 60 day window which is sufficient data coverage for retrieving tidal amplitudes and phases after closing the data gaps in local time by harmonic fits [*Oberheide et al.*, 2013]. This Kp criterion is necessary for NO because NO is very sensitive to solar and geomagnetic activities. On the other hand, CO_2 is less sensitive to the solar and geomagnetic activities and therefore does not require any Kp criterion be introduced in the tidal analysis. A brief description of the data analysis methodology is presented here: 60 days of NO and CO_2 cooling rates data are binned and averaged into 2 hr local time bins for each interval of height (2 km), latitude (5°), and longitude (5°). In the next step, the local time gaps (~ 3 hr within a 60 day period) for a given height and latitude bin are closed by performing harmonic fits in time. These data are then Fourier fit with respect to longitude to get tidal amplitudes and phases on a day-by-day basis. The whole process is stepped forward one day at a time such that these recovered amplitudes and phases represent 60 day running mean averages. Tidal amplitudes and phases are finally averaged into monthly mean bins. NO tidal amplitudes approach the noise level at about 180 km and the diagnostics is thus limited to the 100-180 km altitude range.

2.2 DE2 and DE3 tides in NO and CO_2 Cooling Rates

Figure 1 exemplifies the amplitude spectra of diurnal and semidiurnal nonmigrating tides in the SABER NO and CO_2 cooling rates for September 2013 at 125 km. Migrating tidal components are not shown here as the focus is on the nonmigrating tidal components

originating near the Earth's surface. DE3 is the largest component because of its large vertical wavelength [*Zhang et al.*, 2006] that makes it less likely to dissipate. Other major nonmigrating diurnal components are D0, DW2, DW3, DE2 and DW5. Similarly, the most important nonmigrating semidiurnal components are found to be SE2, SW3, SW1 and SW6. DE3 and DE2 are known to be generated near the Earth's surface due to latent heat release in the deep convective clouds and are among the two most important tides for mesosphere and lower thermosphere (MLT) studies. Note that the tidal spectra can change substantially from one season to another, with, for example, DE2 being very prominent during northern hemisphere winter as discussed later in this section. Furthermore, it is interesting to see that the thermospheric spectra show quite prominent DW5 and SW6 components. These components are observed as zonal wavenumber 4 in the local time frame of a slowly precessing satellite such as TIMED [*Oberheide et al.*, 2003] and frequently neglected when using observed zonal wavenumber 4 signals in satellite observations as a proxy for DE3 and SE2 tidal activity [*Li et al.*, 2015; *Gasperini et al.*, 2017]. The magnitude of the DW5 (roughly 30% of the DE3) is quite surprising as this component has a comparatively shorter vertical wavelength and should be largely dissipated in the thermosphere. However, in the present study our main focus is on tides that originate from the tropospheric weather, and hence we will discuss findings for the DE2 and DE3 components in the following. The diagnostics of other diurnal and semidiurnal components will be performed in the future, including the DW5 component which merits a more detailed investigation on its own.

During our study, it turned out that structural differences between the DE2 and DE3 in the NO and CO_2 cooling rate tides and their seasonal variation come from the corresponding structural differences in the dynamical tide. As such, the underlying physics defining the impact of the solar cycle on the observed DE2 and DE3 cooling rate tides and their tidal drivers remain the same. Hence, we only show figures for the DE3 component throughout this paper and refer the reader to the supporting information section for the DE2 figures, to improve readability.

The height structures of the DE3 (DE2) cooling rate amplitudes and phases in CO_2 and NO for the years 2002-2013 are shown in Figure 2 (Figure S2). The amplitudes are shown as energy loss rates and in percent deviation from the monthly zonal mean. CO_2 DE3 amplitude has a maximum of $\sim$ 46 nW/m^3 at around 100 km whereas DE2 maximizes at a slightly higher altitude with the largest amplitude of $\sim$ 16 nW/m^3. The relative amplitudes of both the DE3 ($\sim$24%) and DE2 ($\sim$10%) generally peak at altitudes slightly higher (2-5 km) than their corresponding absolute amplitudes. Both the DE2 and DE3 amplitudes (absolute and relative) show a considerable seasonal but little inter-annual variations. Phases for both tidal components indicate upward propagation up to 110 km. However, they transition into constant phases above 110 km. *Nischal et al.* [2017] discussed this peculiar behavior of DE2 and DE3 phases in CO_2 cooling rates during solar minimum in detail. It will be further elaborated in section 3.4. A very weak to no solar cycle variation is found in the DE3 and DE2 amplitudes and phases. Both DE3 and DE2 amplitudes in NO cooling rates maximize at around 125 km with peak amplitudes of $\sim$ 1.4 nW/m^3 and $\sim$ 0.6 nW/m^3, respectively. In contrast to the CO_2 case, the relative amplitudes ($\sim$30% for DE3 and $\sim$14% for DE2) are larger and maximize at altitudes slightly lower than 125 km. This is because the maximum zonal mean NO cooling rates are at about 135 km [*Mlynczak et al.*, 2010]. Unlike CO_2, a noticeable solar cycle variation can be seen in the NO DE2 and DE3 tidal amplitudes. However, this variation is much smaller in the relative amplitudes. Different to CO_2, the DE2 and DE3 phases in the NO cooling rates show a clear upward propagating behavior throughout the lower thermosphere region.

Figure 3 (Figure S3) shows the latitudinal structure of the DE3 (DE2) cooling rate amplitudes and phases in CO_2 and NO at 125 km for the years 2002-2013. The DE3 amplitude in CO_2 maximizes around the equator and during late boreal summer with a maximum of $\sim$ 0.7 nW/m^3. The latitudinal structure is generally symmetric about the equator.

The DE2, on the other hand, has a maximum of ~ 0.5 nW/m^3 around boreal winter and is less symmetric about the equator. The amplitudes in percent are ~ 7% and ~ 4% for DE3 and DE2, respectively and they follow the latitudinal structure of absolute amplitudes. It should be noted that these tidal impacts become insignificant at higher latitudes and data are only shown between +/- 40°. Both the DE3 and DE2 amplitudes (absolute and relative) show very weak solar cycle variations. CO_2 cooling rate amplitudes also reveals a quasi-2-year pattern in DE3 amplitudes with relative maxima in years, 2002, 2004, 2006 and 2008 whereas, relative minima in 2003, 2005 and 2007. This alternate maximum and minimum pattern has a phase change after 2008 and hence one can see maxima in 2009 and 2011. Such quasi-2-year variation can be attributed to the Quasi-Biennial Oscillation (QBO) modulation of DE3 tides, primarily around May-August period. This is consistent with previous findings, for example, *Liu et al.* [2017] reports the modulation of tides in temperature and winds by the QBO using Ground-to-topside Atmosphere-Ionosphere model for Aeronomy (GAIA). *Pancheva et al.* [2014] has also reported similar findings in the DE3 tidal fields in mesospheric ozone. El Niño-Southern Oscillation (ENSO) signals can also be observed in the DE3 amplitudes (Figure 3). Although the response of DE3 to El Niño events is very small, La Niña events have a significant impacts on the DE3 tides during winter months. For example, a very high DE3 amplitude in the winter of 2010/2011 around 0-20°S is consistent with findings in *Warner and Oberheide* [2014]. A thorough discussion of QBO and ENSO effects on these nonmigrating tides in the NO and CO_2 emissions is beyond the scope of this paper. In short, the results shown here are generally in good agreement with those reported by previous studies about the impacts of QBO and ENSO on the dynamical tides in mesosphere and lower thermosphere MLT region by previous studies [*Warner and Oberheide*, 2014; *Liu et al.*, 2017].

In comparison to the CO_2 case, the latitudinal structure of DE3 and DE2 amplitudes in NO cooling rates is somewhat broader. However, DE3 (with a peak amplitude of ~1.4 nW/m^3) remains more symmetric about the equator than the DE2 (with a maximum of ~0.8 nW/m^3). The relative amplitudes are on the order of ~18% for DE3 and ~12% for DE2. The latitudinal structure of the DE3 in NO shows a double-peak feature, especially in the relative amplitudes. The seasonal variations of DE3 and DE2 amplitudes are similar to those observed in the CO_2 cooling rates and closely follow the dynamical tides [*Forbes et al.*, 2008].

3 Photochemical Modeling

We perform photochemical modeling to shed light on the large solar cycle variation of NO cooling rate tides and small one of CO_2. The tidal diagnostic of SABER cooling rates showed that the observed DE2 and DE3 amplitudes in NO cooling rates exhibit a significant solar cycle dependence whereas those in CO_2 emission have weak to no solar cycle dependence. Photochemical modeling also helps to understand why the absolute and relative amplitudes show different degrees of solar cycle variation. In addition, it will provide insights into how the contributions from the individual tidal drivers (temperature, density and advection) vary over as function of the solar cycle. While the overall approach follows previous solar minimum works on NO [*Oberheide et al.*, 2013] and CO_2 [*Nischal et al.*, 2017] photochemical modeling, the current work also implements changes in the model background and vertical tidal advection scheme. For details of the modeling methodology, see the abovementioned papers. Here, we will focus on the parts which differ from the previously used methodology.

Thermospheric NO 5.3 μm and CO_2 15 μm emissions are largely the result of inelastic collision between NO or CO_2 molecules with atomic oxygen [*Mlynczak et al.*, 2010]. Hence, any change in the amount of emitted 5.3 μm and 15 μm radiation is due to the change in NO or CO_2 abundances, change in O abundance, and the change in temperature. The latter is because the rate of collisional excitation of NO or CO_2 molecules depends on temperature. Furthermore, tidal modulation of any one or all of these parameters will

result in a longitudinal/local time modulation of NO and CO_2 infrared emissions in the thermosphere.

To perform the photochemical modeling and separate the individual tidal drivers, we compute NO 5.3 μm volume emission rate (VER) as follows [*Winick et al.*, 1987]:

$$VER = h\nu A_{5.3\mu m}[NO]_{v=1} \tag{1}$$

$$[NO]_{v=1} = \left(\frac{S_E + k_{NO-O}e^{-2700/T}[O]}{A_{5.3\mu m} + k_{NO-O}[O]}\right)[NO]_{v=0} \tag{2}$$

where photon energy hν is equal to $\sim 3.75 \times 10^{-20}$ J, S_E is the earthshine and equal to 1.06×10^{-4} s^{-1} [*Caledonia and Kennealy*, 1982], k_{NO-O} is the rate coefficient for the deactivation of NO by O and equal to 2.8×10^{-11} cm^{-3}/s [*Dodd et al.*, 1999] and $A_{5.3\mu m}$ is the Einstein's coefficient and equal to 12.54 s^{-1}.

Similarly, CO_2 cooling rate resulting from the fundamental band transition (v_2), that is, the CO_2 ($01^10 \rightarrow 00^00$), is calculated following *Wise et al.* [1995]:

$$VER = h\nu A_{15\mu m}[CO_2](01^10) \tag{3}$$

$$[CO_2](01^10) = \left(\frac{J_R + 2k_{CO_2-O}e^{-960/T}[O]}{A_{15\mu m} + k_{CO_2-O}[O]}\right)[CO_2](00^00) \tag{4}$$

with hν equal to $\sim 1.36 \times 10^{-22}$ J, J_R is the radiative excitation rate due to other (00^10) photons, k_{CO_2-O} is the rate coefficient for the deactivation of CO_2 by O and equal to $3.5(\pm 1.8) \times 10^{-13}\sqrt{T} + 2.32 \times 10^{-9}$ exp(-76.75/$T^{1/3}$) cm^{-3} $molecule^{-1}$ s^{-1} [*Sharma and Wintersteiner*, 1990] and $A_{15\mu m}$ = 1.28 s^{-1}. By setting J_R equal to zero in equation 4, equation 3 gives an approximation for CO_2 cooling rates. The rate coefficient used in the calculation of both the NO and CO_2 cooling rates are the ones used in the SABER temperature retrieval [*Mlynczak et al.*, 2010].

3.1 Background Data

For the photochemical modeling, unperturbed backgrounds (i.e., monthly mean zonal mean [NO], [CO_2], [O], temperature) are required in addition to tidal perturbations. Because of the lack of observations in the thermosphere, we make use of a combination of observations and empirical models in order to build continuous background profiles. See *Nischal et al.* [2017] for the details. Briefly, we combine [O], T and neutral density from the SABER version 2.0 data set [*Mlynczak et al.*, 2010] with those from NRLMSISE-00 [*Picone et al.*, 2002]. We use SABER observations of atomic oxygen, temperature and neutral density up to 95 km. Above this altitude, NRLMSISE-00 profiles are scaled in a way that they follow SABER profiles as closely as possible. Examples for the resulting O volume mixing ratio (VMR) and T profiles are shown in Figures 4a and 4b. This method of building a background profile is possible because the vertical gradients of O, T, and neutral density in NRLMSISE-00 and SABER are very similar [*Nischal et al.*, 2017]. It should be emphasized that the leading goal of the photochemical modeling is not to achieve a one-to-one match with the observation, but to separate the different tidal drivers and to study their relative contributions toward imposing the tidal impacts on the NO or CO_2 cooling rates. *Nischal et al.* [2017] reported the sensitivity of the computed zonal mean cooling rates to the choice of the background. The results indicate that although the magnitude of absolute tidal amplitudes obtained using different background vary, the general amplitude structure remain the same. That is, the uncertainties in the model background are not really important. CO_2 volume mixing ratio (VMR) comes from daytime SABER observation. SABER 2C data set released by SABER (http://saber.gats-inc.com/) provides CO_2 and temperature up to 140 km, where above 110 km, CO_2 volume mixing

ratio (VMR) and temperature profiles are supplied by the WACCM model [*Rezac et al.*, 2015]. For NO density, we use the Nitric Oxide Empirical Model (NOEM), which is an empirical model based on Student Nitric Oxide Explorer (SNOE) observations and employs the method of empirical orthogonal functions to derive the NO density in the thermosphere as a function of altitude (100-150 km) and latitude (80°N-80°S) [*Marsh et al.*, 2004]. This is different to *Oberheide et al.* [2013] who used a MIPAS/ENVISAT NO density background. The ENVISAT mission ended in early 2012.

The next step is to introduce tidal perturbations in these background parameters ([O], [CO_2], [NO], neutral density and T). This is done by using tidal dynamics from an empirical tidal model, the Climatological Tidal Model of the Thermosphere (CTMT) [*Oberheide et al.*, 2011a,b], which provides well validated definitions of the DE2 and DE3 tides in the thermosphere based on TIMED observations in the MLT region. We employ the solar cycle dependent CTMT version [*Oberheide et al.*, 2011b] which reproduces the solar cycle dependence of thermospheric tides observed by the CHAMP satellite well. *Oberheide et al.* [2013] and *Nischal et al.* [2017] used vertical wind tides from CTMT for the computation of vertical tidal advection of [O], [NO], and [CO_2]. Here, we use adiabatic vertical displacement theory ([*Eckermann et al.*, 1998; *Ward*, 1999; *Smith et al.*, 2010]). The reason why the adiabatic displacement theory can be applied in the computation of nonmigrating tides in the background parameters and how this method is advantageous over the vertical tidal advection approach is as follows.

3.2 Adiabatic Displacement Theory

The approach is based on the vertical displacement δz of an air parcel from its equilibrium height. Without any net production/loss rate and without diffusion/dissipation/breaking, the two continuity equations (one for the total number density, n and the other for constituent number density, n_i) yield

$$\frac{dq}{dt} = 0 \tag{5}$$

where $q = n_i/n$ is the constituent volume mixing ratio and d/dt is the material derivative. This results in a constant q within a displaced air parcel. Thus, a region of unique constituent mixing ratio traces the Lagrangian motion of an air parcel [*Eckermann et al.*, 1998]. The vertical constituent velocity w'_q is clearly identical to the atmospheric velocity w' in this case.

In the case with diffusion/dissipation/breaking, however, w'_q and w' are no longer the same, as for example, the molecular diffusion coefficient is different for different species [*Chabrillat et al.*, 2002] and the difference between these two velocities increases with altitude because the diffusive time scale equals the tidal period at about 140 km [*Müller-Wodarg and Aylward*, 1998]. As a result, the use of w' from CTMT in previous studies, *Oberheide et al.* [2013] and *Nischal et al.* [2017], namely using w', as a proxy for w'_q is somewhat questionable. CTMT accounts for diffusion/dissipation/breaking but does not provide individual constituent velocities. In the following we show that T' from CTMT and adiabatic displacement theory provides a better approximation for w'_q than using w' from the model

The thermal energy equation with diffusion terms (f) can be approximated as [*Forbes*, 1982]

$$\frac{dT}{dt} = (\gamma - 1)\frac{T}{n}\frac{dn}{dt} + f \tag{6}$$

where $\gamma = c_p/c_v$ is the ratio of the specific heats at constant pressure and volume. After linearization, equation 6 results in

$$\frac{\partial T'}{\partial t} + w'(\frac{g}{c_p} + \frac{\partial \bar{T}}{\partial z}) = \frac{f'}{c_v} \tag{7}$$

where the prime indicates the tidal perturbation, bar indicates the mean and g is the altitude dependent gravity. It can be shown [*Forbes*, 1982] that f′ on the right hand side of equation 7 approximates to

$$f' = \frac{\partial K}{\partial z}\frac{\partial T'}{\partial z} + K\frac{\partial^2 T'}{\partial z^2} \tag{8}$$

where K = K_0 + $\bar{n}K_{eddy}$ with molecular thermal conductivity, K_0 and eddy thermal conductivity, K_{eddy}. The second order term in equation 8 can be neglected and to a good approximation, the first term as well, because of the long vertical wavelength of the DE2 and DE3 tides in the thermosphere. Thermal diffusion causes the vertical displacement associated with the temperature perturbation T′ to be somewhat less than for a purely adiabatic motion [*Gardner*, 2018]. With these approximations, equation 7 becomes

$$\frac{\partial T'}{\partial t} + w'(\frac{g}{c_p} + \frac{\partial \bar{T}}{\partial z}) = 0 \tag{9}$$

such that adiabatic displacement theory applies [*Eckermann et al.*, 1998; *Ward*, 1999] and the δz can be approximated as

$$\delta z = -\left(\frac{T'}{\Gamma + \Gamma_{ad}}\right) \tag{10}$$

where, Γ = g/c_p is the local lapse rate and $\Gamma_{ad} = \partial\bar{T}/\partial z$ is the adiabatic lapse rate, $w'_q = \partial\delta z/\partial t$.

Using adiabatic displacement is still an approximation, however, it yields more realistic tidal variation than w′ from CTMT. The perturbation mixing ration q′ resulting from the adiabatic displacement of an air parcel from its equilibrium position z_1 to a z_2 such that δz = z_2 - z_1, is given by [*Eckermann et al.*, 1998]

$$q'(z_2) = q(z_2) - \bar{q}(z_2) = \bar{q}(z_1) - \bar{q}(z_2) \tag{11}$$

because q remains constant within the displaced air parcel. For a linear background $\bar{q}(z_2) = \bar{q}(z_1) + (\partial\bar{q}/\partial z)\ \delta z$. Equation 11 thus results in

$$q' = q'(z_2) = -(\frac{\partial \bar{q}}{\partial z})\delta z \tag{12}$$

with q as either the O or NO or CO_2 mixing ratio.

To test the sensitivity of the modeling results to the choice of methodology (adiabatic displacement or vertical advection using w′), we use data from a TIME-GCM [*Roble and Ridley*, 1994] September equinox run in order to compute tidal perturbations in NO and CO_2 VMR and VER using both the advection and adiabatic approach. We then compare these results with those coming directly from the TIME-GCM run ("true" results). The results for DE3 amplitudes and phases in CO_2 and NO VMR are shown in Figure 5. DE3 VMR amplitudes computed using the adiabatic displacement approach (red curve) better match the true TIME-GCM results, particularly at altitudes below 140 km. Above

140 km, the f′=0 approximation in Equation 8 becomes increasingly questionable, resulting in the larger amplitude and phase differences. However, these difference are not important for our study as the bulk of the CO_2 and NO emissions occur at altitudes below 140 km (Figure 2).

To further test the two methods, we calculate the total NO and CO_2 cooling rate amplitudes and phases using TIME-GCM data and the photochemical modeling, that is using Equations 1-4. All parameters (tidal variations and backgrounds) are from TIME-GCM and results shown in Figure 6 are the sum of tidal temperature, density and vertical advection/adiabatic displacement effects on the cooling rates. While the overall impact of the latter on the amplitudes and phases is not large, the vertical advection approach nevertheless produces better results for NO around the peak altitude of 115 km including a better match of the phase, and also for CO_2. Amplitudes above 140 km are generally unchanged while phase changes in this altitude regime are not significant due to the small amplitudes. A similar result is obtained for DE2 (not shown). Hence, all the photochemical modeling results presented in the following use adiabatic displacement. They are still referred to as "vertical advection" to reflect the physical mechanism.

3.3 Modeled DE2 and DE3 in NO and CO_2 Cooling Rates

Similar to *Oberheide et al.* [2013] and *Nischal et al.* [2017], all the photochemical modeling results presented hereafter have been computed by linearizing (using multivariate Taylor series) equations 2 and 4, in terms of temperature, density and displacement effect. This is because the tidal diagnostic approach applied in section 2.1 is inherently linear. This allows us to directly compare the observed and modeled tides, and to identify the coupling mechanisms.

Figure 7 (Figure S4) shows the DE3 (DE2) height structure of amplitudes and phases in CO_2 and NO cooling rates from the photochemical modeling using the background described in section 3.1 and CTMT dynamical tides. Photochemical model reproduces the observed CO_2 tidal amplitude and phase structures (compare Figures 2 and S2), including their seasonal variations. The modeled absolute amplitudes are larger than in observations. This systematic difference is within the uncertainty introduced by the uncertainty in the background profiles, particularly atomic oxygen, as discussed in *Nischal et al.* [2017] for solar minimum conditions. Consequently, the systematic difference between the modeled and observed relative amplitudes is much smaller. In addition, the photochemical model also reproduces the observed phase slope transitions in the CO_2 DE2 and DE3 phases at $\sim$ 110 km. The modeling results also replicate the weak solar variations observed in the CO_2 amplitudes and phases.

The modeled NO tidal amplitudes and phases match with the observations as well (compare Figures 2 and S2). Absolute NO tidal amplitudes are also on the high side of observed results in the height structure. This also applies to the relative amplitudes, in contrast to the CO_2 case. A possible source of generally larger modeled NO amplitudes can be the NO background used in the photochemical modeling. Moreover, the modeled DE3 and DE2 absolute amplitudes peak at slightly higher altitude ($\sim$ 5 km). Since the peak altitude in the relative amplitudes is about the same in the observed and modeled results, this can also be attributed to the NO background. Model also reproduces the observed solar cycle variations of the NO cooling rate amplitudes. Phases agree well with the SABER results.

The modeled latitudinal structures of the DE3 (DE2) at 125 km in CO_2 and NO cooling rates are Figure 8 (Figure S5). Both absolute and relative CO_2 and NO amplitudes are in very good agreement with their corresponding observed parts (compare Figures 3 and S3). Overall, the agreement between the observed and modeled results is very good. Systematic amplitude differences can be attributed to the uncertainty in the background

model parameters, especially atomic oxygen. They do not impact the discussion of the relative importance of the different tidal coupling mechanisms.

4 Discussion

4.1 Tidal Coupling Mechanisms

The photochemical modeling now allows us to understand how the tidal coupling mechanisms respond to the solar cycle and to contrast the results with the solar minimum studies by *Oberheide et al.* [2013] and *Nischal et al.* [2017]. Figure 9 exemplifies the results for the DE3 tides in CO_2 cooling rates for the year 2008 and 2013. These results are obtained by switching the corresponding tidal variations on and off in our linearized photochemical modeling. The aim is to separate the individual contributions of different tidal drivers. Because systematic differences do not matter for this discussion, it is sufficient to compare normalized amplitudes. Temperature is the main tidal driver throughout the lower thermosphere because Equation 2 is highly dependent on temperature. However, the neutral density contribution starts competing with the contribution from temperature at higher altitudes (upward of 110 km) and as such explains the observed phase slope transition around 110 km (thick black line shifting towards the density curve in Figure 9b) because the contribution from temperature and density are almost out of phase. The contribution from vertical advection is relatively small. Results for the DE2 component (Figure S6) are consistent with these findings. The 2008 DE3 results only differ in minor details from those in *Nischal et al.* [2017], due to the change of the vertical advection computation. A new result is the solar maximum year 2013 coupling mechanisms in Figures 9c and 9d. The relative contributions do not change much from solar minimum to maximum, as one might expect because the dynamical tides (temperature, density, winds) do not respond in an appreciable manner to solar activity in the mesosphere/ lower thermosphere region [*Oberheide et al.*, 2009]. Phases are unaffected by the solar cycle.

In the thermosphere, however, upward propagating dynamical tides respond strongly to the solar cycle, mostly due to the temperature dependence of thermal conductivity which is a major contributor to tidal dissipation. As discussed in *Oberheide et al.* [2009], solar minimum DE3 tides above $\sim$ 120 km are approximately 60% larger in temperature, up to a factor of five in density, but only $\sim$ 10% larger in vertical wind, as compared to solar maximum conditions. For the NO case, one might thus expect a resulting large change in the relative importance of the coupling mechanisms as a function of solar cycle with vertical advection becoming more important during solar maximum, density much less important, and also a reduced importance of temperature. However, Figure 10 indicates that this not the case. Temperature near the peak emission altitude of $\sim$ 125 km becomes even more important during solar maximum, despite the smaller tidal temperature amplitudes, and the same is found for density. The relative vertical advection contribution, on the other hand, decreases above 130 km. Phases are not impacted by the solar cycle. Clearly, solar cycle dependent changes in the background conditions in temperature, and nitric oxide and atomic oxygen density overcompensate for the solar cycle effect in the dynamical tides and require a more detailed discussion. The individual tidal drivers show similar characteristics in the DE2 results (Figure S7).

These results show that the temperature, advection and density are the leading coupling mechanism and hence the observed tides in the NO and CO_2 cooling rates can be a good proxy for studying tidal activity in thermosphere where global tidal observations are sparse. For example, NO 5.3 μm cooling rate tidal phases can be used to study the seasonal and solar cycle variation of temperature tides in the thermosphere. This can lead to the understanding of tidal dissipation parameterizations in the various tidal models.

4.2 Solar Cycle Dependence of Nitric Oxide Cooling Rate Tides

Figure 11 details the time evolution of individual driver contributions to the absolute (left) and relative (right) DE3 NO cooling rate tides shown in Figure 7. Plotted are the NO cooling rate amplitudes due to tidal temperature, density and advection, respectively, in absolute units (left column) and with respect to the monthly mean zonal mean NO cooling rate, that is, the relative amplitudes (right column). Phases are not shown as they remain unaffected by the solar cycle. The overall solar cycle pattern in the contributions from all three drivers, that is, much larger absolute amplitudes (left column) during solar maximum, is due to the ~factor of eight solar cycle dependence of the NO cooling rate in the zonal mean [*Mlynczak et al.*, 2010]. This large dependence of the mean is not overcome by the larger dynamical DE3 tides during solar minimum, which are caused by the $T^{2/3}$ dependence of thermal conductivity, which is a major contributor to tidal dissipation in the thermosphere. However, the solar cycle dependence of the advection contribution is less pronounced as compared to the temperature and density contributions. This is not only due to the lower sensitivity of vertical tidal winds in the thermosphere to the solar cycle but also due to the larger vertical gradients in the NO VMR (Figure 4d) during solar minimum. Consequently, an essentially unchanged vertical tidal wind acts on a larger gradient, producing a relative increase of tidal NO cooling rates that partly balances the impact of the generally lower NO cooling rate amplitudes. The result is the increasing relative importance of tidal advection (as compared to temperature and density) during solar minimum and the decreasing importance during solar maximum seen in Figure 10. Changes in atomic oxygen VMR gradients also contribute but to a lesser extent as they do not vary much from solar minimum to solar maximum (Figure 4a).

Above ~ 120 km, the relative DE3 NO amplitudes from all drivers maximize during solar minimum, although the effect is rather weak and within one color scale. This is due to the abovementioned larger dynamical tides ~120 km during solar minimum while the effect of the solar cycle in the mean NO emission rates vanishes in the relative amplitudes. Compared to the absolute amplitudes, the relative amplitudes from all three drivers do not show any appreciable solar cycle dependence at altitudes below ~ 120 km and only a weak one at altitudes above. This is consistent with the lack of an appreciable DE3 solar cycle signal in the dynamical tides below ~ 120 km [*Oberheide et al.*, 2009] and mean temperature (Figure 4b), and the rather small atomic oxygen and nitric oxide VMR solar cycle signals in this altitude regime. The results for DE2 component (not shown here) are consistent with these findings.

The apparent two-year signal in the temperature and density contributions from 2002-2009 of about two color scales (peak-to-peak) is the result of the QBO in the equatorial DE3 tide in temperature and density. *Oberheide et al.* [2009] reported a 15-20% (peak-to-peak) QBO signal which is quantitatively consistent with the two color scale signal in Figure 11 (right) since background temperature and density do not change much from one year to another below 120 km (Figure 4). In 2010-2011, the QBO signal in Figure 11 is distorted by an El Niño/Southern Oscillation (ENSO) signal in the dynamical DE3 [*Warner and Oberheide*, 2014], particularly during the winter 2010/11 La Niña, before restoring to the regular QBO pattern. Note that vertical tidal winds are less sensitive to the QBO which explains the absence of a clear signal in the advection contribution. These results are consistent with those detailed in the section 2.

4.3 Relative Importance of NO and CO_2 Cooling Rate Tides for the Energy Budget of the Lower Thermosphere during solar minimum/maximum

The nonmigrating tidal signal in CO_2 15 μm emissions have little to no solar cycle dependence whereas those in NO 5.3 μm emissions vary significantly over a solar cycle. Nevertheless, both NO and CO_2 cooling rate tides are important to the energy budget of the lower thermosphere. Figure 12 quantifies the relative contributions of NO and CO_2

cooling rate tides to the longitudinal/local time modulation of the thermospheric infrared emissions over a of full solar cycle. Figure 12a compares the relative importance of the DE3 NO and CO_2 cooling rate tides for the infrared energy budget of the lower thermosphere during solar minimum and solar maximum. During solar minimum conditions (solid lines), NO tides remain relatively unimportant primarily because there is little NO produced so that background is very low whereas, CO_2 tides play a major role. However, during solar maximum (dotted lines), NO DE3 tides become more important above 135 km compared to the CO_2 tides. The results for the DE2 (Figure 12b) component show a similar characteristic, although the NO DE2 tides during solar maximum overtakes the CO_2 tides at much lower altitude of 120 km.

5 Conclusions

The solar cycle variation of two important nonmigrating tides, the DE3 and DE2, in NO 5.3 μm and CO_2 15 μm infrared cooling rates has been studied. SABER NO and CO_2 cooling rate data for 2002-2013 were analyzed to obtain nonmigrating tidal amplitudes and phases a function of altitude, latitude and year. Photochemical modeling was performed using CTMT dynamical tides and backgrounds from SABER, NRLMSISE-00 and NOEM to separate the individual tidal drivers and understand the structure and causes of solar cycle variations in the observed tidal amplitudes. The main conclusions are as follows:

1. Tidal diagnostics of SABER cooling rate data show that the DE2 and DE3 tides from tropospheric convection strongly modulate the NO at 5.3 μm and CO_2 at 15 μm emissions. Amplitudes are on the order of 15% (DE2) and 30% (DE3) relative to the monthly zonal mean. Supporting photochemical modeling reproduces the observed results, including the seasonal and inter-annual variations. Systematic amplitude differences between the observed and modeled results can be attributed to the uncertainty in the model backgrounds, especially, the atomic oxygen and do not impact the conclusion on physical mechanism. Phases match well with the observations.

2. CO_2 cooling rate tides show a very weak solar cycle dependence. Smaller temperature tides and larger CO_2 cooling rate background during solar maximum largely compensate for each other. The relative contribution from the individual tidal drivers do not change much from solar minimum to maximum as the dynamical tides remain somewhat unresponsive to the solar activity in the MLT region. Phases remain unaffected by the solar cycle.

3. On the other hand, nonmigrating tidal amplitudes (absolute) in NO cooling rates show a significant ($\sim$ factor of 10) solar cycle variation as the small NO cooling rate background is not overcome by the larger dynamical tides during solar minimum. Relative amplitudes show a rather weak solar cycle dependence, however, they are larger during solar minimum. The relative importance of the coupling mechanism also shows solar cycle variations, most notably, the importance of the tidal advection contribution increases during solar minimum and decreases during solar maximum. Phases do not show any solar cycle dependence.

4. NO cooling rate tides largely remain unimportant for the longitudinal modulation of infrared energy budget of the lower thermosphere during solar minimum conditions as compared to CO_2. However, they become very important during solar maximum above 135 km for DE3 and above 120 km for DE2.

5. Observed tides in the infrared cooling in the thermosphere can be a suitable proxy for studying the tidal height evolution and its solar cycle dependence in the thermosphere where there is a significant lack of global temperature observations. For example, NO 5.3 μm tidal phase is a good proxy for temperature phase and can be utilized to improve dissipation parameterizations in tidal models.

Acknowledgments

All SABER data used are available from the SABER data repository at http://saber.gats-inc.com/. The NOEM and CTMT models are documented in the given references. NRLMSISE-00 is available through the community coordinated modeling center at https://ccmc.gsfc.nasa.gov/. Data files to produce the Figures are archived at Clemson University and available upon request. N. N and J. O were supported by a grant from the National Science Foundation (NSF) Aeronomy Program, Award AGS-1112704.

References

Akmaev, R. A., T. J. Fuller-Rowell, F. Wu, J. M. Forbes, X. Zhang, A. F. Anghel, M. D. Iredell, S. Moorthi, and H. Juang (2008), Tidal Variability in the lower thermosphere: comparison of Whole Atmosphere Model (WAM) simulations with observations from TIMED, *Geophys. Res. Lett., 35*, L03810, doi:10.1029/2007GL032584.

Caledonia, C.E., and J.P. Kennealy (1982), NO infrared emission in the upper atmosphere, *Planet. Space Sci., 30*, 1043–1056.

Chabrillat, S., G. Kockarts, D. Fonteyn, and G. Brasseur (2002), Impact of molecular diffusion on the CO2 distribution and the temperature in the mesosphere, *Geophys. Res. Lett., 29* (15), doi: 10.1029/2002GL015309, 2002.

Chang, L. C., C.-H. Lin, J. Yue, J.-Y. Liu, and J.-T. Lin (2013), Stationary planetary wave and nonmigrating tidal signatures in ionospheric wave 3 and wave 4 variations in 2007-2011 FORMOSAT-3/COSMIC observations, *J. Geophys. Res., Space Phys., 118*, 6651-6665, doi:10.1002/jgra.50583.

Curtis, A. R., and R. M. Goody (1956), Thermal radiation in the upper atmosphere, *Proc. R. Soc. London, Ser., A*, *236*, 193-206.

Dodd, J.A., R.B. Lockwood, E.S. Hwang, S.M. Miller, and S.J. Lipson (1999), Vibrational relaxation of NO(=1) by oxygen atoms, *J. Chem. Phys., 111*, 3498–3507.

Eckermann, S. D., D. E. Gibson-Wilde, and J. T. Bacmeister (1998), Gravity wave perturbations of minor constituents: A parcel advection methodology *J. Atmos. Sci. 55*, (24), 3521–3539.

England, S. L., T. J. Immel, D. Huba, M. E. Hagan, A. Maute, and R. DeMajistre (2010), Modeling of multiple effects of atmospheric tides on the ionosphere: An examination of possible coupling mechanisms responsible for the longitudinal structure of the equatorial ionosphere, *J. Geophys. Res., 115*, A05308, doi:10.1029/2009JA014894.

England, S. L. (2005), A review of the effects of non-migrating atmospheric tides on the Earth's low-latitude ionosphere, *Space Sci. Rev., 168*, 211-236, doi:10.1007/s11214-011-9842-4.

Flynn, S., D. J. Knipp, T. Matsuo, M. G. Mlynczak, and L. Hunt (2018). Understanding the global variability in thermospheric nitric oxide flux using empirical orthogonal functions (EOFs), *Journal of Geophysical Research: Space Physics, 123*, 4150–4170, doi:10.1029/2018JA025353.

Forbes, J. M. (1982), Atmospheric tides: 1. Model description and results for the solar diurnal component, *J. Geophys. Res., 87* (A7), 5222–5240, doi: 10.1029/JA087iA07p05222.

Forbes, J. M., D. Wu (2006), Solar tides as revealed by measurements of mesopshere temperature by the MLS experiment on UARS, *J. Atmos. Sci., 63*(7), 1776-1797.

Forbes, J. M., X. Zhang, S. Palo, J. Russell, C. J. Mertens, and M. G. Mlynczak (2008), Tidal Variability in the ionospheric dynamo region, *J. Geophys. Res., 113*, A02310, doi:10.1029/2007JA012737.

Forbes, J. M., S. L. Bruinsma, X. Zhang, and J. Oberheide (2009), Surface-exosphere coupling due to thermal tides, *Geophys. Res. Lett., 36*, L15812, doi: 10.1029/2009GL038748.

Gasperini, F., M. E. Hagan, and Y. Zhao (2017), Evidence of tropospheric 90 day oscillations in the thermosphere, *Geophysical Research Letters, 44*, 10,125–10,133.

https://doi.org/10.1002/2017GL075445

Gardner, C. S. (2018). Role of wave-induced diffusion and energy flux in the vertical transport of atmospheric constituents in the mesopause region. *Journal of Geophysical Research: Atmospheres, 123*, 6581–6604. https://doi.org/10.1029/2018JD028359

Hagan, M. E., A. Maute, R. G. Roble, A. D. Richmond, T. J. Immel, and S. L. England (2007), Connections between deep tropical clouds and the Earth's ionosphere, *Geophys. Res. Lett., 34*, L20109, doi:10.1029/2007GL030142.

Hagan, M. E., A. Maute, R. G. Roble (2007), Tropospheric tidal effects on the midle and upper atmosphere, *J. Geophys. Res., 114*, 1302, doi:10.1029/2008JA013637.

Häusler, K., H. Lühr, S. Rentz, and W. Köhler (2007), A statistical analysis of longitudinal dependence of upper thermospheric zonal winds at dip equator latitudes derived from CHAMP, *J. Atmos. Sol. Terr. Phys., 69*(12), 1419-1430, 10.1016/j.jastp.2007.04.004

Häusler, K., and H. Lühr (2009), Nonmigrating tidal signal in the upper thermospheric zonal wind at equatorial latitudes as observed by CHAMP, *Ann. Geophys., 27*, 2643-2652, doi:10.5194/angeo-27-2643-2009.

Häusler, K., H. Lühr, M. E. Hagan, A. Maute, and R. G. Roble (2010), Comparison of CHAMP and TIME-GCM nonmigrating tidal signals in the thermospheric zonal wind, *J. Geophys. Res., 115*, D00I08, doi: 10.1029/2009JD012394.

Häusler, K., J. Oberheide, H. Lühr, and R. Koppmann (2013), The Geospace response to nonmigrating tides, in *Climate and Weather of the Sun-Earth System (CAWSES): Highlights from a Priority Program*, edited by F.-J. Lübken, 481-506, Springer Atmospheric Sciences, Dordrecht, Heidelberg, New York, London, doi:10.1007/978-94-007-4348-9.

Immel, T. J., E. Sagawa, S. L. England, S. B. Henderson, M. E. Hagan, S. B. Mende, H. U. Frey, C. M. Swenson, and L. J. Paxton (2006), Control of equatorial ionospheric morphology by atmospheric tides, *Geophys. Res. Lett., 33*(L15108), doi:10.1029/2006GL026161.

Jones, M. Jr., J. M. Forbes, and M. Hagan (2016), Solar cycle variability in mean thermospheric composition and temperature induced by atmospheric tides, *J. Geophys. Res. Space Physics, 121*, 5837-5855, doi:10.1002/2016JA022701

Kockarts, G. (1980), Nitric oxide cooling in the terrestrial thermosphere, *Geophys. Res. Lett.*, *7*, 137-140, doi:10.1029/GL007i002p00137.

Li, X., W. Wan, Z. Ren, L. Liu, and B. Ning (2015), The variability of nonmigrating tides detected from TIMED/SABER observations, *J. Geophys. Res. Space Physics, 120*, 10,793–10,808, doi: 10.1002/2015JA021577.

Liu, H., Y.-Y. Sun, Y. Miyoshi, and H. Jin (2017), ENSO effects on MLT diurnal tides: A 21 year reanalysis data-driven GAIA model simulation, *J. Geophys. Res. Space Physics, 122*, 5539-5549, doi:10.1002/2017JA024011.

Lühr, H., K. Häusler, C. Stolle, (2007), Longitudinal variation of F region electron density and thermospheric zonal wind caused by atmospheric tides, *Geophys. Res. Lett. 34*, 16,102, doi: 10.1029/2007GL030639.

Lühr, H., M. Rother, K. Häusler, P. Alken, and S. Mauss (2008), The influence of nonmigrating tides on the longitudinal variation of the equatorial electrojet, *J. Geophys. Res., 113*, A08313, doi: 10.1029/2008JA013064.

Marsh, D. R., S. C. Solomon, and A. E. Reynolds (2004), Empirical model of nitric oxide in the lower thermosphere, *J. Geophys. Res., 109*, A07301, doi: 10.1029/2003JA010199.

Mlynczak, M., et al. (2003) The natural thermostat of nitric oxide emission at 5.3 m in the thermosphere observed during the solar storms of April 2002, *Geophys. Res. Lett., 30*, 2100, doi: 10.1029/2003GL017693, 21.

Mlynczak, M. G., et al. (2010), Observations of infrared radiative cooling in the thermosphere on daily to multiyear time scales from the TIMED/SABER instrument, *J. Geophys. Res., 115*, A03309, doi:10.1029/2009JA014713.

Müller-Wodarg, I., and A. D. Aylward (1998), The inuence of tides on composition of the thermosphere, *Adv. Space Res., 21*, 807–810, doi:10.1016/S0273-1177(97)00678-9.

Nischal, N., J. Oberheide, M. G. Mlynczak, L. A. Hunt, and A. Maute (2017), Non-migrating tidal impact on the CO_2 15 μm infrared cooling of the lower thermosphere during solar minimum conditions, *J. Geophys. Res., 122*, 6761-6775, doi:10.1002/2017JA024273.

Oberheide, J., M. E. Hagan, and R. G. Roble (2003), Tidal signatures and aliasing in temperature data from slowly precessing satellites, *J. Geophys. Res., 108*, 1055, doi:10.1029/2002JA009585, A2.

Oberheide, J., and J. M. Forbes (2008), Thermospheric nitric oxide variability induced by nonmigrating tides, *Geophys. Res. Lett., 35*, L16814, doi:10.1029/2008GL034825.

Oberheide, J., J. M. Forbes, K. Häusler, Q. Wu, and S, L, Bruinsma (2009), Tropospheric tides from 80-400 km: propagation, interannual variability, and solar cycle effects, *J. Geophys. Res., 114*, D00I05, doi:10.1029/2009JD012388.

Oberheide, J., J. M. Forbes, X. Zhang, and S. L. Bruinsma (2011), Climatology of upward propagating diurnal and semidiurnal tides in the thermosphere, *J. Geophys. Res., 116*, A11306, doi:10.1029/2011JA016784.

Oberheide, J., J. M. Forbes, X. Zhang, and S. L. Bruinsma (2011), Wave-driven variability in the ionosphere-thermosphere-mesosphere system from TIMED observations: What contributes to the "wave 4"?, *J. Geophys. Res., 116*, A01306, doi:10.1029/2010JA015911.

Oberheide, J., M. G. Mlynczak, C. N. Mosso, B. M. Schroeder, B. Funke, A. Maute (2013), Impact of tropospheric tides on the nitric oxide 5.3 μm infrared cooling of the low-latitude thermosphere during solar minimum conditions, *J. Geophys. Res., 118*, 7283-7293, doi:10.1002/2013JA019278.

Pancheva, D., P. Mukhtarov, A. K. Smith (2014), Nonmigrating tidal variability in the SABER/TIMED mesospheric ozone, *Geophys. Res. Lett., 41*, 4059-4067, doi:10.1002/2014GL059844.

Pedatella, N. M., and H.-L. Liu (2013), Influence of the El Niño Southern Oscillation on the middle and upper atmosphere, *J. Geophys. Res. Space Physics, 118*, 2744–2755, doi: 10.1002/jgra.50286.

Picone, J. M., A. E. Hedin, D. P. Drob, and A. C. Aikin (2002), NRLMSISE-00 empirical model of the atmosphere: Statistical comparisons and scientific issues, *J. Geophys. Res., 107*(A12), 1468, doi:10.1029/2002JA009430.

Rezac, L., et al. (2015), Validation of the global distribution of CO_2 volume mixing ratio in the mesopshere and lower thermosphere from SABER, *J. Geophys. res. Atmos., 120*, 12,067-12,081, doi:10.1002/2015JD023995.

Roble, R. G., and E. C. Ridley (1994), A thermosphere-ionosphere-mesosphere-electrodynamics general circulation model (TIME-GCM): equinox solar minimum simulations (30-500 km), *Geophys. Res. Lett., 21*, 417-420.

Russell, J. M. III, M. G. Mlynczak, L. L. Gordley, J. Tansock, and R. Esplin (1999), An overview of the SABER experiment and preliminary calibration results, *Proc SPIE Int. Soc. Opt. Eng., 3756*, 277-288, doi:10.1117/12.366382.

Sagawa, E., T. J. Immel, H. U. Frey, and S. B. Mende (2005), Longitudinal structure of the equatorial anomaly in the nighttime ionosphere observed by IMAGE/FUV, *J. Geophys. Res., 110*, A11302, doi:10.1029/2004JA010848.

Siskind, D. E., et al. (2019), On the relative roles of dynamics and chemistry governing the abundance and diurnal variation of low-latitude thermospheric nitric oxide, *Ann. Geophys., 37*, 37-48, doi: 10.5194/angeo-37-37-2019.

Sharma, R. D., and P. P. Wintersteiner (1990), Role of carbon dioxide in cooling planetary atmospheres, *Geophys. Res. Lett., 17*, 2201.

Smith, A. K., D. R. Marsh, M. G. Mlynczak, and J. C. Mast (2010), Temporal variations of atomic oxygen in the upper mesosphere from SABER, *J. Geophys. Res., 115*, D18309, doi: 10.1029/2009JD013434.

Talaat, E. R., and R. S. Lieberman (2010), Direct Observations of nonmigrating diurnal tides in the equatorial thermospehere, *Geophys. Res. Lett. 37*, L04803,

doi:10.1029/2009GL041845.

Ward, W. E., (1999), A simple model of diurnal variations in the mesospheric oxygen nightglow, *Geophys. Res. Lett. 26*, (23), 3565–3568, doi:10.1029/1999GL003661.

Warner, K., J. Oberheide (2014), Nonmigrating tidal heating and MLT tidal wind variability due to the El Nino-Southern Oscillation, *J. Geophys. Res. Atomos., 119* 1249-1265, doi:10.1002/2013JD020407.

Winick, J.R., R.H. Picard, R.A. Joseph, R.D. Sharma, and P.P. Wintersteiner (1987), An infrared spectral radiance code for the auroral thermosphere (AARC), *Tech. Rep.* AFGL-TR- 87-0334, Air Force Geophys. Lab., Hanscom Air Force Base, Mass.

Wise, J. O., et al. (1995), CIRRIS 1A global observation of 15-μm CO_2 and 5.3-μm NO limb radiance in the lower thermosphere during moderate to active geomagnetic activity, *J. Geophys. Res., 100*, 21,357-21,373, doi:10.1029/95JA02053.

Zhang, X., J. M. Forbes, M. E. Hagan, J. M. Russell III, S. E. Palo, C. J. Mertens, and M. G. Mlynczak (2006), Monthly tidal temperatures 20-120 km from TIMED/SABER, *J. Geophys. Res., 111*, A10S08, doi:10.1029/2005JA011504.

Zhang, Y., S. England, L. J. Paxton (2010), Thermospheric composition variations due to nonmigrating tides and their effect on ionosphere, *Geophys. Res. Lett., 37*, L17103, doi:10.1029/2010GL044313.

Figure 1. Spectra of nonmigrating tides versus latitude for September 2013 at 125 km. (a) Diurnal tides in NO cooling rates. (b) Semidiurnal tides in NO cooling rates. (c) Diurnal tides in CO_2 cooling rates. (d) Semidiurnal tides in CO_2 cooling rates. Negative wave numbers represent eastward propagating waves and positive wave numbers correspond to westward propagating waves. Note that migrating tides are omitted in the spectra.

Figure 2. DE3 amplitudes and phases in CO_2 (left) and NO (right) cooling rates vector averaged over +/- 20° for 2002-2013 from SABER. (a) CO_2 DE3 amplitudes in 10^{-9} W/m^3. (b) CO_2 DE3 amplitudes in percent deviation from the monthly zonal mean. (c) CO_2 DE3 phases in local time of maximum. (d) NO DE3 amplitudes in 10^{-9} W/m^3. (e) NO DE3 amplitudes in percent deviation from the monthly zonal mean. (f) NO DE3 phases in local time of maximum. White areas indicate data gaps because of the Kp-criterion for NO.

Figure 3. DE3 amplitudes and phases in CO_2 (left) and NO (right) cooling rates at 125 km for 2002-2013 from SABER. (a) CO_2 DE3 amplitudes in 10^{-9} W/m^3. (b) CO_2 DE3 amplitudes in percent deviation from the monthly zonal mean. (c) CO_2 DE3 phases in local time of maximum. (d) NO DE3 amplitudes in 10^{-9} W/m^3. (e) NO DE3 amplitudes in percent deviation from the monthly zonal mean. (f) NO DE3 phases in local time of maximum. White areas indicate data gaps because of the Kp-criterion for NO.

Figure 4. Monthly mean zonal mean profiles at the equator for September (2002-2008). (a) Atomic oxygen volume mixing ratio (VMR) from SABER and NRLMSISE00. (b) Temperature from SABER and NRLMSISE00. (c) Carbon dioxide VMR from SABER. (d) Nitric oxide VMR from NOEM.

Figure 5. DE3 amplitudes and phases at the equator in CO_2 and NO volume mixing ratio (VMR) using TIME-GCM September equinox data. Plotted as blue curves are results computed using the vertical tidal advection approach, and red curves are computed using the adiabatic displacement method. Overplotted as black lines are the "true" results from the TIME-GCM run. (a) DE3 amplitudes in CO_2 VMR. (b) DE3 phases in CO_2 VMR. (c) DE3 amplitudes in NO VMR. (d) DE3 phases in NO VMR.

Figure 6. DE3 amplitudes and phases at the equator in CO_2 and NO cooling rates using TIME-GCM September equinox data. Plotted as blue curves are results computed using the vertical tidal advection approach, and red curves are computed using the adiabatic displacement method. Overplotted as black lines are the "true" results from the TIME-GCM run. (a) DE3 amplitudes in CO_2 cooling rates. (b) DE3 phases in CO_2 cooling rates. (c) DE3 amplitudes in NO cooling rates. (d) DE3 phases in NO cooling rates.

Figure 7. Same as Figure 2 but from the photochemical modeling.

Figure 8. Same as Figure 3 but from the photochemical modeling. Note that white gaps represent represent missing data.

Figure 9. (a) Normalized September DE3 amplitudes in the CO_2 cooling rates at the equator from photochemical modeling. Shown are the total (all) response and the individual responses due to temperature, density, and advection. Overplotted as "+" line is the SABER observation. Normalization is with respect to the maximum of the "all" curve ("all" curve represents when all the tidal variations are switched on in the photochemical modeling) for the model output and with respect to the maximum of the observation. (b) Corresponding DE3 phases. The top panel (a,b) is for year for 2008 and the bottom panel (c,d) for 2013.

Figure 10. Same as Figure 9 but for NO.

Figure 11. Contributions from temperature, density and advection in the NO DE3 cooling rate tides at equator. (a) Temperature amplitudes in 10^{-9} W/m^3. (b) Density amplitudes in 10^{-9} W/m^3. (c) Advection amplitudes in 10^{-9} W/m^3. (d) Temperature amplitudes in percent deviation from the monthly zonal mean. (e) Density amplitudes in percent deviation from the monthly zonal mean. (f) Advection amplitudes in percent deviation from the monthly zonal mean.

Figure 12. (a) September DE3 amplitudes in 10^{-9} W/m^3 in NO (red) and CO_2 (black) cooling rate at the equator for solar minimum year, 2008 (solid line) and solar maximum, 2013 (dotted line). (b) Same as (a) but for DE2 component.

Figure 1.

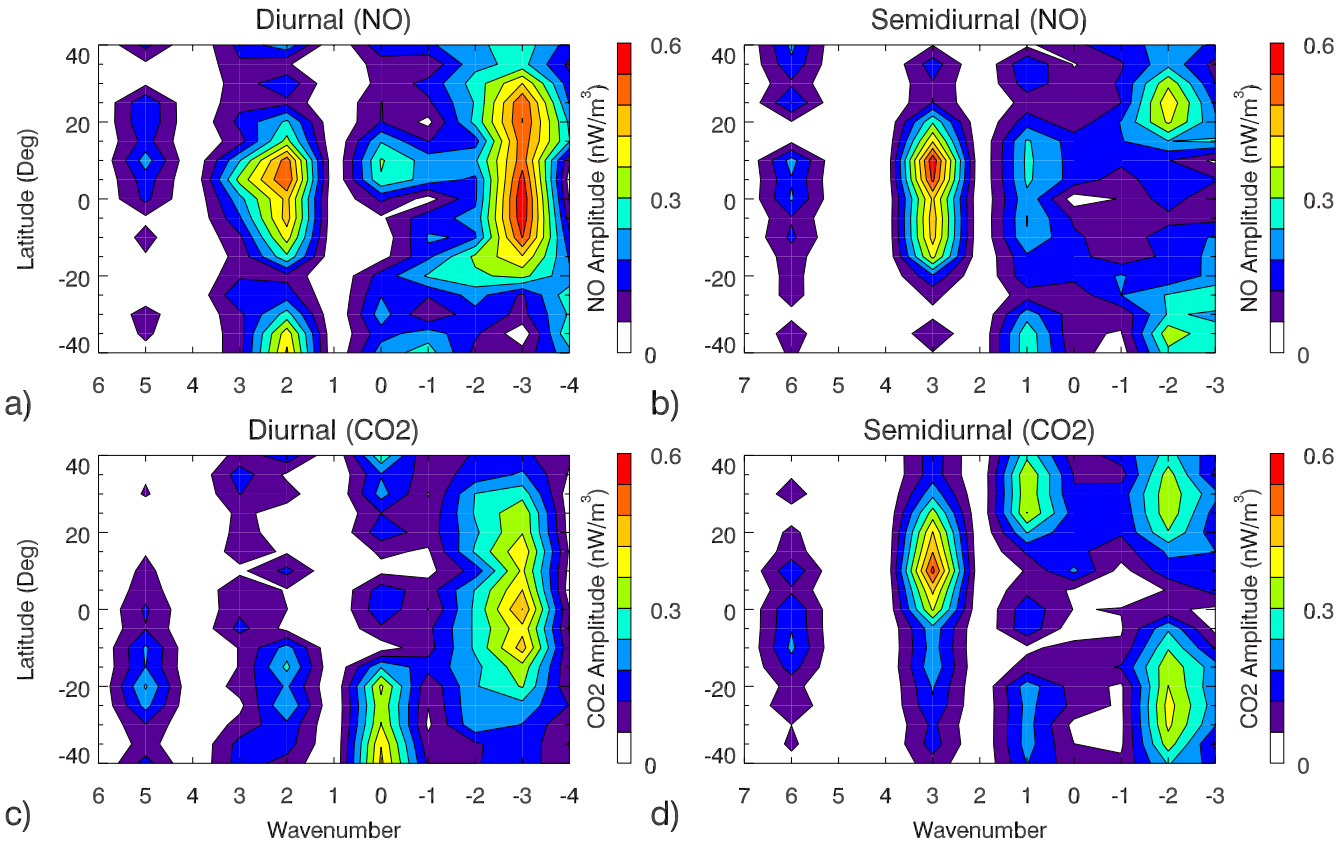
Diurnal (NO)
Semidiurnal (NO)
Diurnal (CO2)
Semidiurnal (CO2)
Latitude (Deg)
Wavenumber
NO Amplitude (nW/m3)
CO2 Amplitude (nW/m3)
a)
b)
c)
d)

Figure 2.

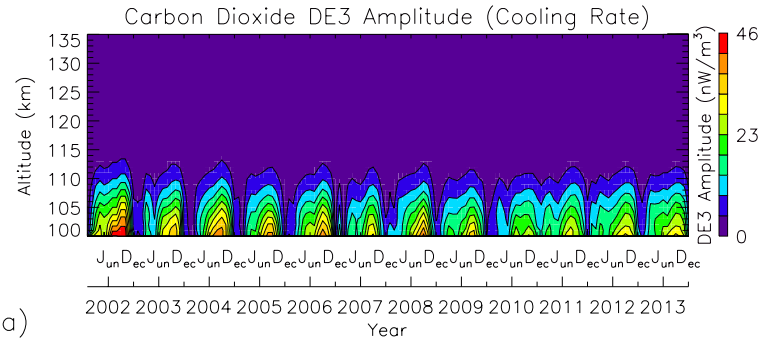
Carbon Dioxide DE3 Amplitude (Cooling Rate)
Altitude (km)
135
130
125
120
115
110
105
100
DE3 Amplitude (nW/m3)
46
23
0
Jun Dec Jun Dec
2002 2003 2004 2005 2006 2007 2008 2009 2010 2011 2012 2013
Year

a)

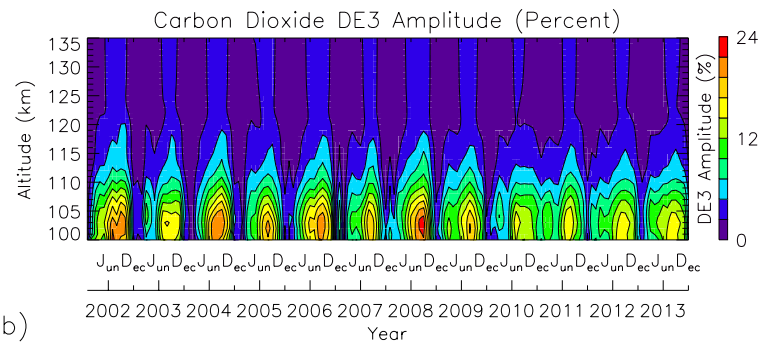
Carbon Dioxide DE3 Amplitude (Percent)
Altitude (km)
135
130
125
120
115
110
105
100
DE3 Amplitude (%)
24
12
0
Jun Dec Jun Dec
2002 2003 2004 2005 2006 2007 2008 2009 2010 2011 2012 2013
Year

b)

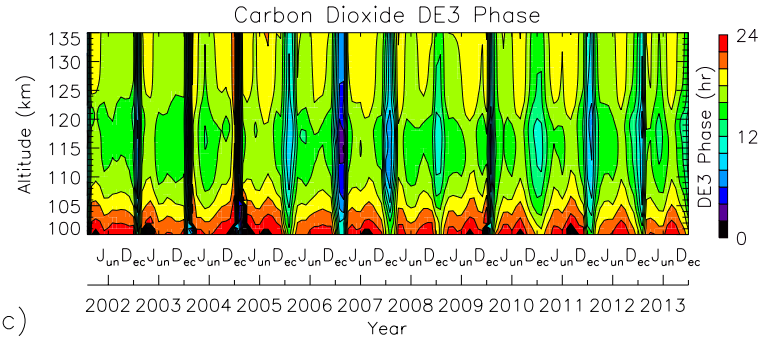
Carbon Dioxide DE3 Phase
Altitude (km)
135
130
125
120
115
110
105
100
DE3 Phase (hr)
24
12
0
Jun Dec Jun Dec
2002 2003 2004 2005 2006 2007 2008 2009 2010 2011 2012 2013
Year

c)

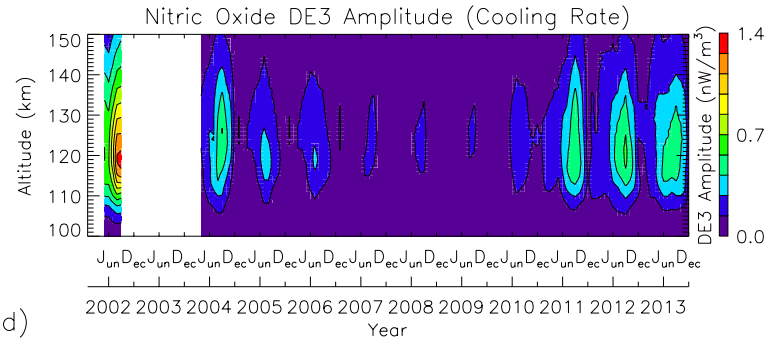
Nitric Oxide DE3 Amplitude (Cooling Rate)
Altitude (km)
150
140
130
120
110
100
DE3 Amplitude (nW/m3)
1.4
0.7
0.0
Jun Dec Jun Dec
2002 2003 2004 2005 2006 2007 2008 2009 2010 2011 2012 2013
Year

d)

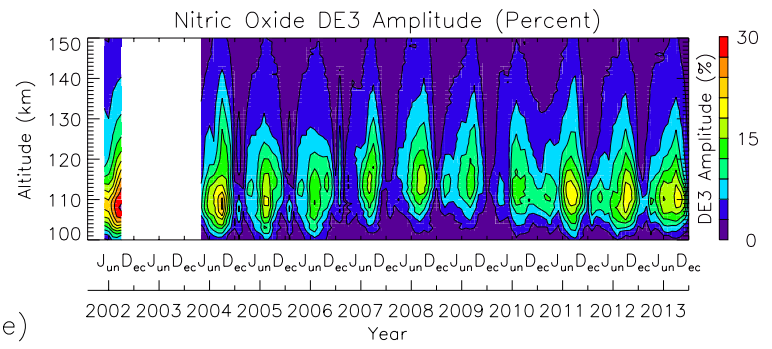
Nitric Oxide DE3 Amplitude (Percent)
Altitude (km)
150
140
130
120
110
100
DE3 Amplitude (%)
30
15
0
Jun Dec Jun Dec
2002 2003 2004 2005 2006 2007 2008 2009 2010 2011 2012 2013
Year

e)

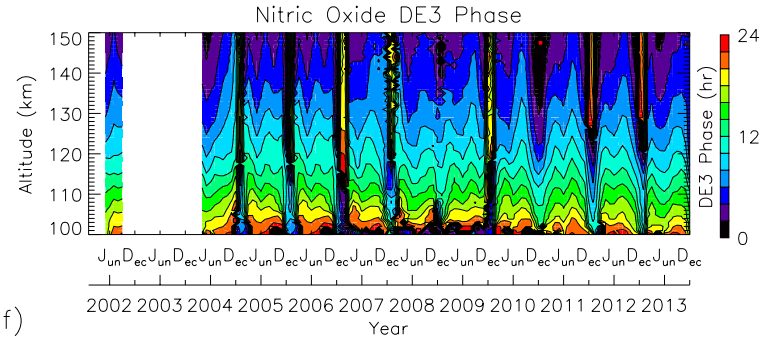
Nitric Oxide DE3 Phase
Altitude (km)
150
140
130
120
110
100
DE3 Phase (hr)
24
12
0
Jun Dec Jun Dec
2002 2003 2004 2005 2006 2007 2008 2009 2010 2011 2012 2013
Year

f)

Figure 3.

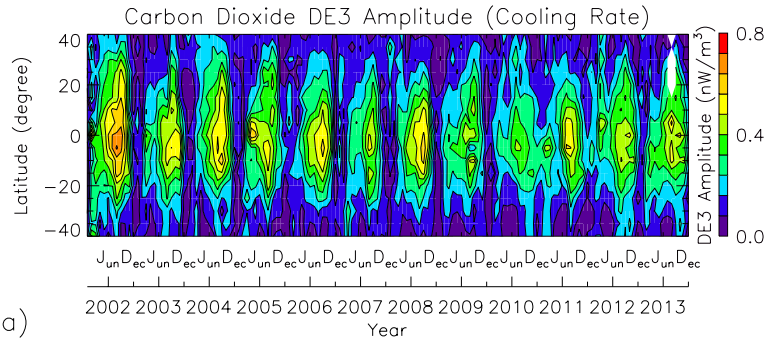
Carbon Dioxide DE3 Amplitude (Cooling Rate)
Latitude (degree)
40
20
0
−20
−40
DE3 Amplitude (nW/m3)
0.8
0.4
0.0
Jun Dec Jun Dec
2002 2003 2004 2005 2006 2007 2008 2009 2010 2011 2012 2013
Year

a)

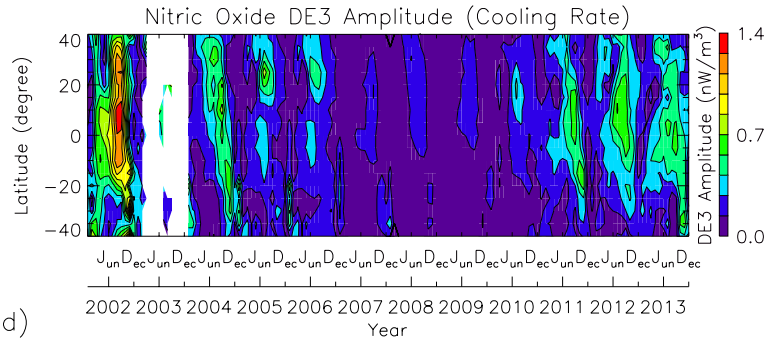
Nitric Oxide DE3 Amplitude (Cooling Rate)
Latitude (degree)
40
20
0
−20
−40
DE3 Amplitude (nW/m3)
1.4
0.7
0.0
Jun Dec Jun Dec
2002 2003 2004 2005 2006 2007 2008 2009 2010 2011 2012 2013
Year

d)

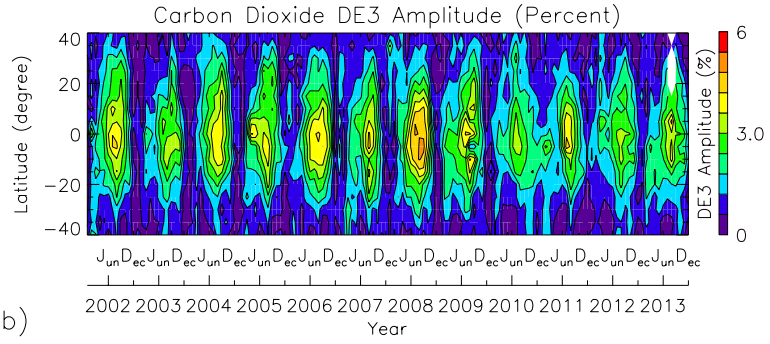
Carbon Dioxide DE3 Amplitude (Percent)
Latitude (degree)
40
20
0
−20
−40
DE3 Amplitude (%)
6
3.0
0
Jun Dec Jun Dec
2002 2003 2004 2005 2006 2007 2008 2009 2010 2011 2012 2013
Year

b)

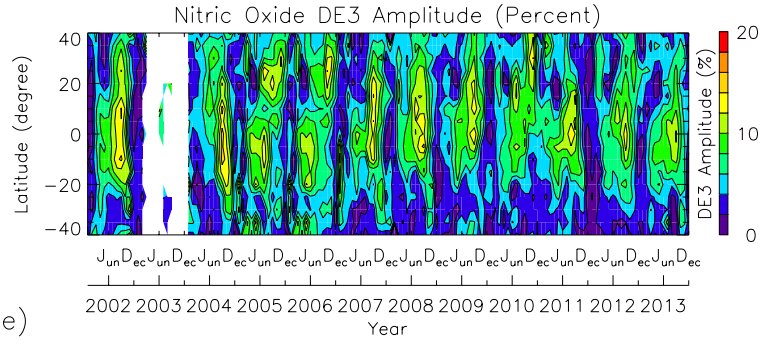
Nitric Oxide DE3 Amplitude (Percent)
Latitude (degree)
40
20
0
−20
−40
DE3 Amplitude (%)
20
10
0
Jun Dec Jun Dec
2002 2003 2004 2005 2006 2007 2008 2009 2010 2011 2012 2013
Year

e)

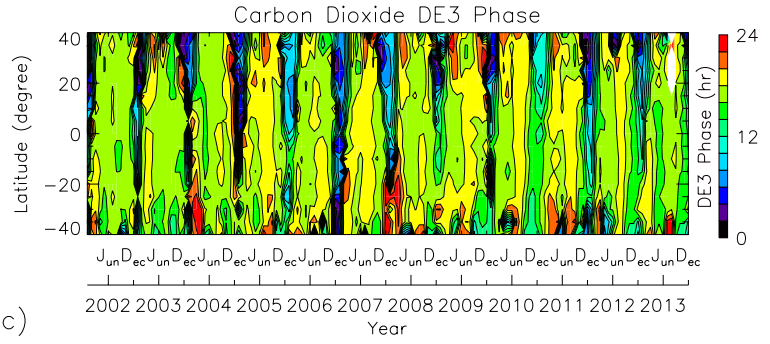
Carbon Dioxide DE3 Phase
Latitude (degree)
40
20
0
−20
−40
DE3 Phase (hr)
24
12
0
Jun Dec Jun Dec
2002 2003 2004 2005 2006 2007 2008 2009 2010 2011 2012 2013
Year

c)

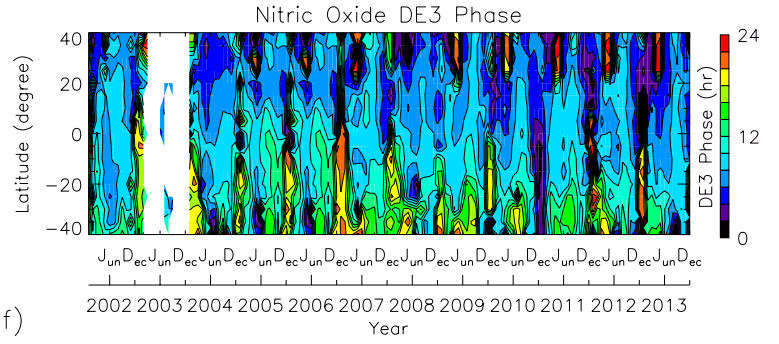
Nitric Oxide DE3 Phase
Latitude (degree)
40
20
0
−20
−40
DE3 Phase (hr)
24
12
0
Jun Dec Jun Dec
2002 2003 2004 2005 2006 2007 2008 2009 2010 2011 2012 2013
Year

f)

Figure 4.

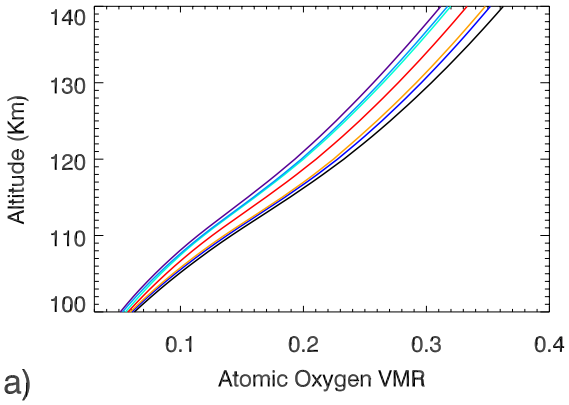
Altitude (Km)
140
130
120
110
100
0.1
0.2
0.3
0.4
Atomic Oxygen VMR

a)

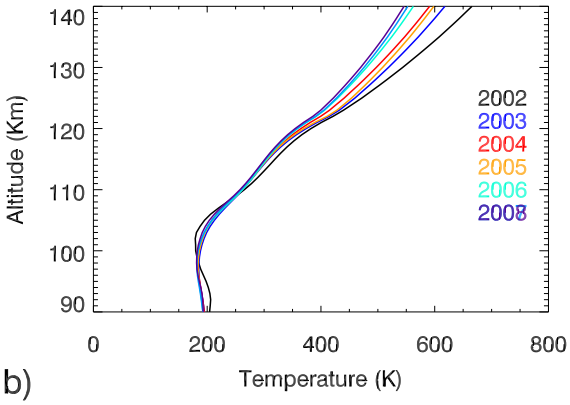
Altitude (Km)
140
130
120
110
100
90
0
200
400
600
800
Temperature (K)
2002
2003
2004
2005
2006
2008

b)

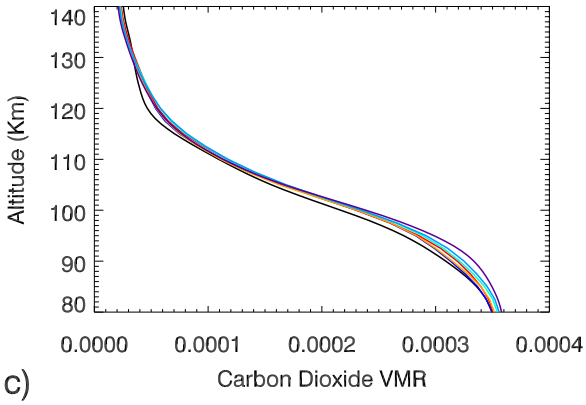
Altitude (Km)
140
130
120
110
100
90
80
0.0000
0.0001
0.0002
0.0003
0.0004
Carbon Dioxide VMR

c)

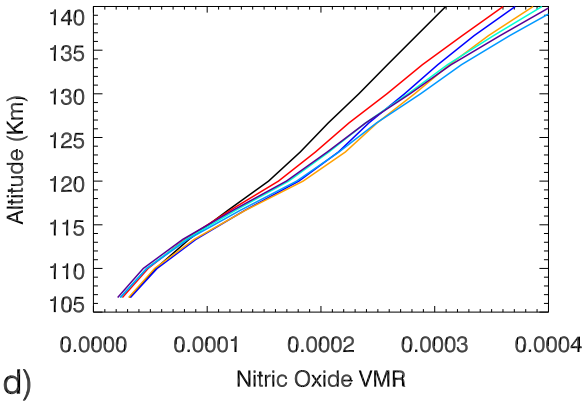
Altitude (Km)
140
135
130
125
120
115
110
105
0.0000
0.0001
0.0002
0.0003
0.0004
Nitric Oxide VMR

d)

Figure 5.

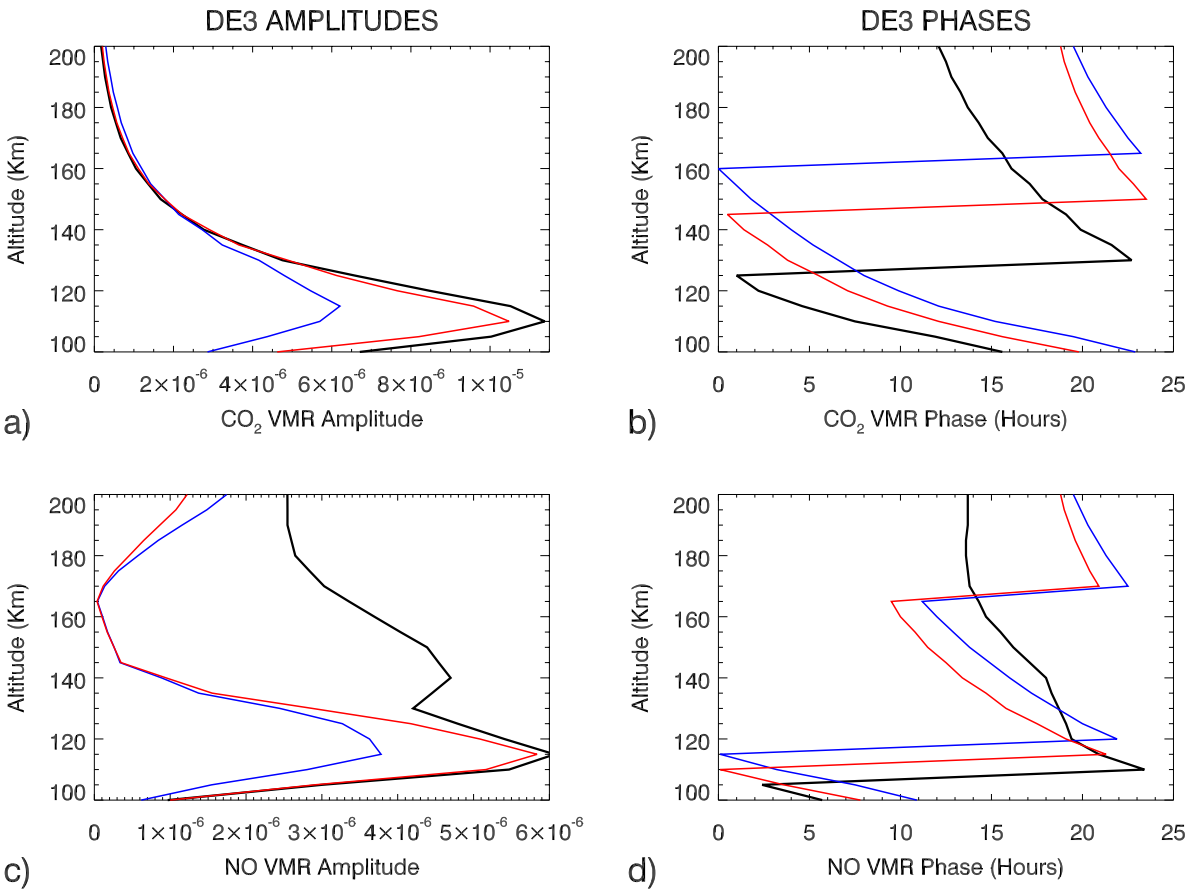
DE3 AMPLITUDES
DE3 PHASES
Altitude (Km)
200
180
160
140
120
100
0
2×10-6
4×10-6
6×10-6
8×10-6
1×10-5
CO2 VMR Amplitude
a)
5
10
15
20
25
CO2 VMR Phase (Hours)
b)
1×10-6
2×10-6
3×10-6
4×10-6
5×10-6
6×10-6
NO VMR Amplitude
c)
NO VMR Phase (Hours)
d)

Figure 6.

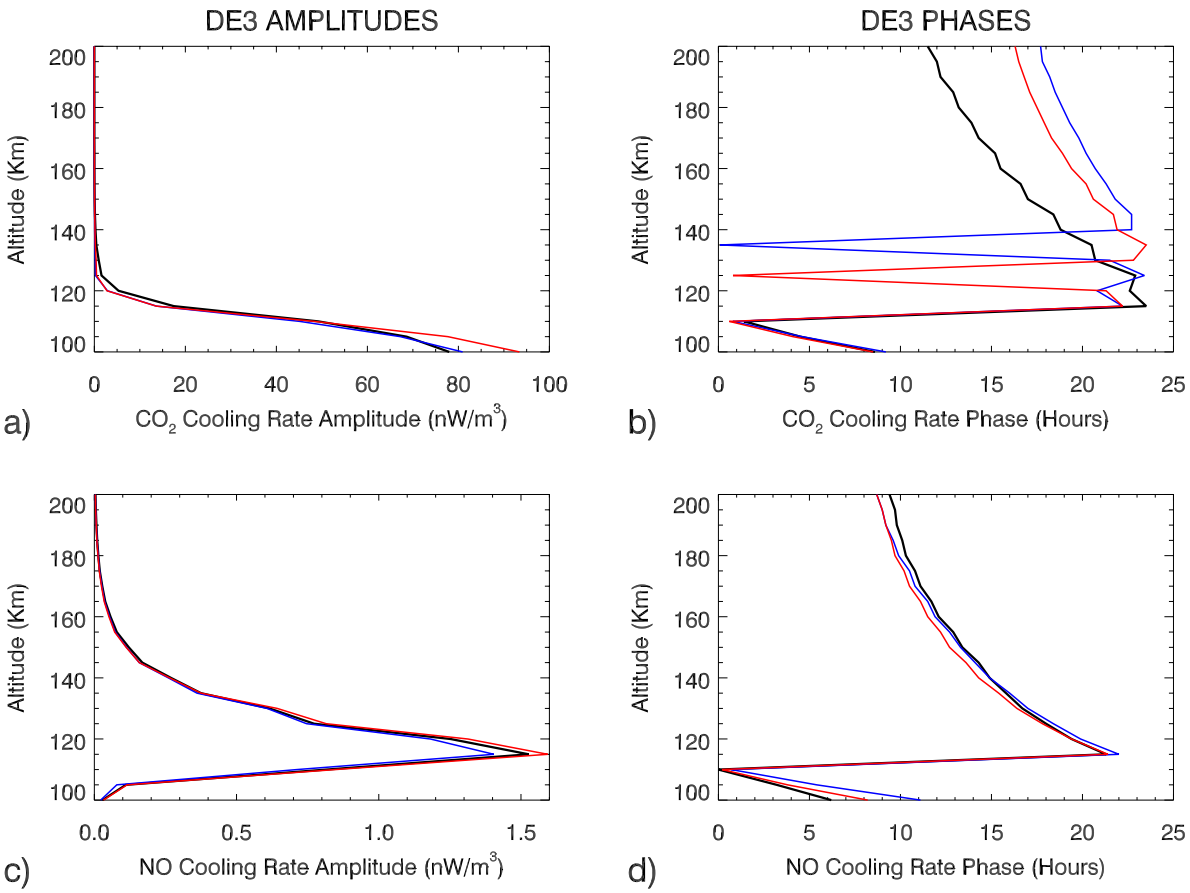
DE3 AMPLITUDES
DE3 PHASES
Altitude (Km)
200
180
160
140
120
100
0
20
40
60
80
100
5
10
15
20
25
a)
b)
c)
d)
CO_2 Cooling Rate Amplitude (nW/m^3)
CO_2 Cooling Rate Phase (Hours)
NO Cooling Rate Amplitude (nW/m^3)
NO Cooling Rate Phase (Hours)
0.0
0.5
1.0
1.5

Figure 7.

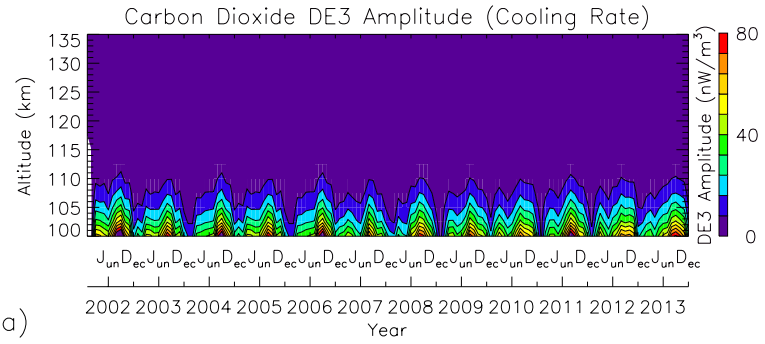
Carbon Dioxide DE3 Amplitude (Cooling Rate)
Altitude (km)
DE3 Amplitude (nW/m3)
Year
a)

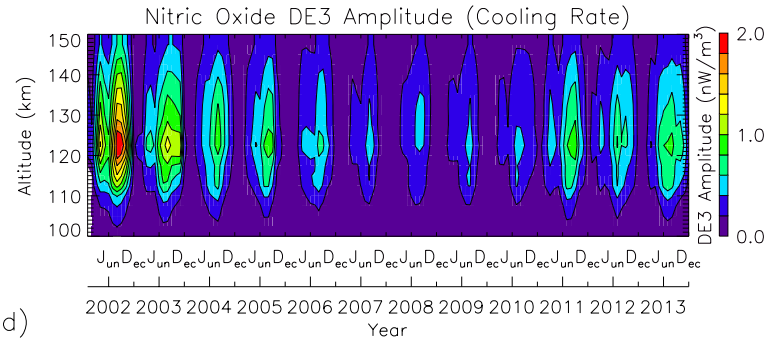
Nitric Oxide DE3 Amplitude (Cooling Rate)
Altitude (km)
DE3 Amplitude (nW/m3)
Year
d)

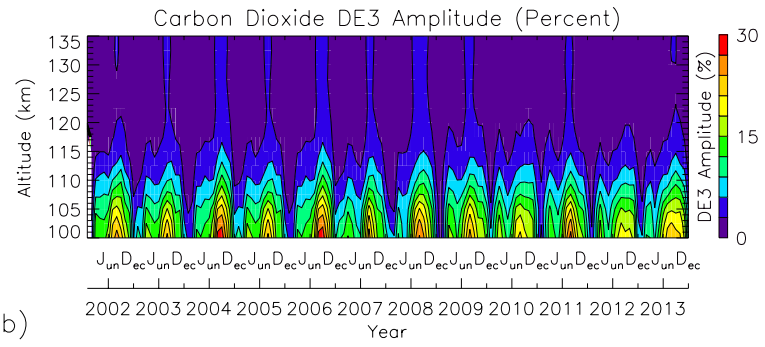
Carbon Dioxide DE3 Amplitude (Percent)
Altitude (km)
DE3 Amplitude (%)
Year
b)

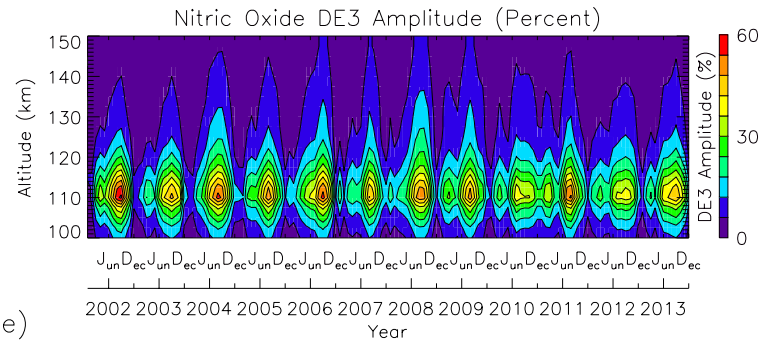
Nitric Oxide DE3 Amplitude (Percent)
Altitude (km)
DE3 Amplitude (%)
Year
e)

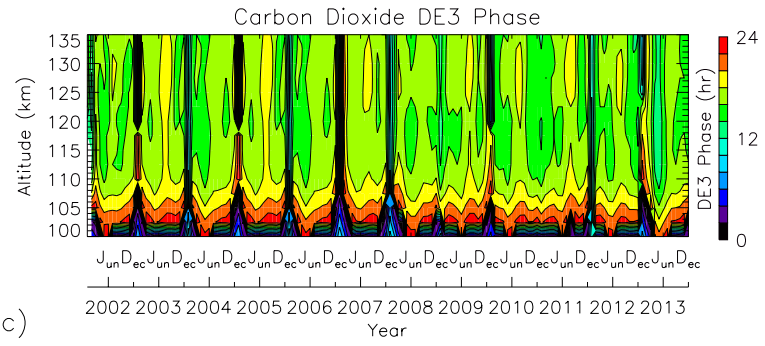
Carbon Dioxide DE3 Phase
Altitude (km)
DE3 Phase (hr)
Year
c)

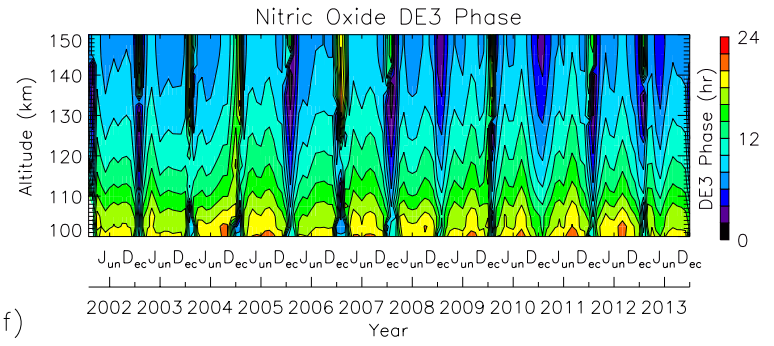
Nitric Oxide DE3 Phase
Altitude (km)
DE3 Phase (hr)
Year
f)

Figure 8.

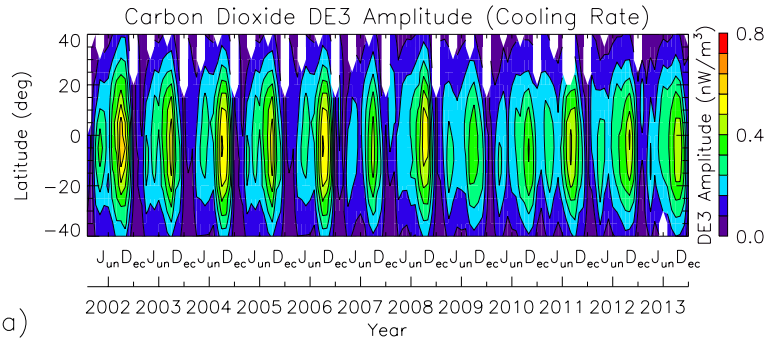
Carbon Dioxide DE3 Amplitude (Cooling Rate)
Latitude (deg)
40
20
0
−20
−40
DE3 Amplitude (nW/m³)
0.8
0.4
0.0
Jun Dec Jun Dec
2002 2003 2004 2005 2006 2007 2008 2009 2010 2011 2012 2013
Year

a)

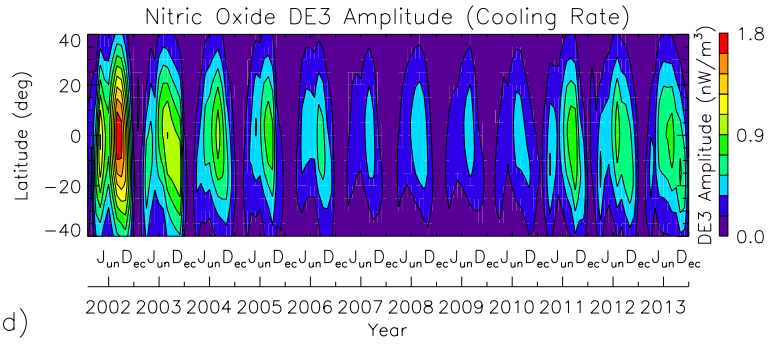
Nitric Oxide DE3 Amplitude (Cooling Rate)
Latitude (deg)
40
20
0
−20
−40
DE3 Amplitude (nW/m³)
1.8
0.9
0.0
Jun Dec Jun Dec
2002 2003 2004 2005 2006 2007 2008 2009 2010 2011 2012 2013
Year

d)

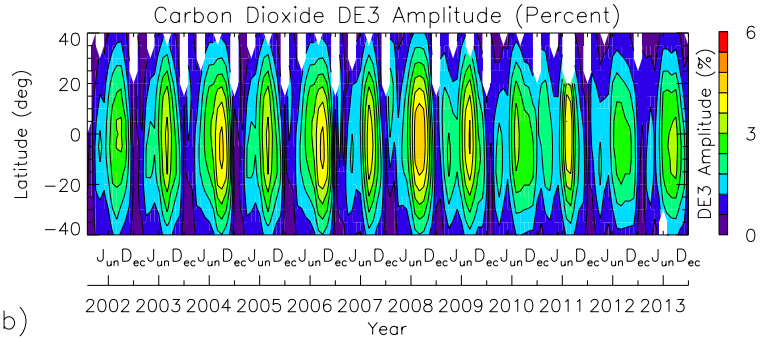
Carbon Dioxide DE3 Amplitude (Percent)
Latitude (deg)
40
20
0
−20
−40
DE3 Amplitude (%)
6
3
0
Jun Dec Jun Dec
2002 2003 2004 2005 2006 2007 2008 2009 2010 2011 2012 2013
Year

b)

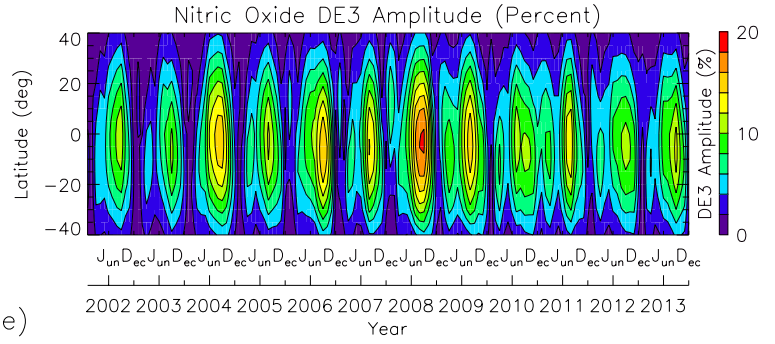
Nitric Oxide DE3 Amplitude (Percent)
Latitude (deg)
40
20
0
−20
−40
DE3 Amplitude (%)
20
10
0
Jun Dec Jun Dec
2002 2003 2004 2005 2006 2007 2008 2009 2010 2011 2012 2013
Year

e)

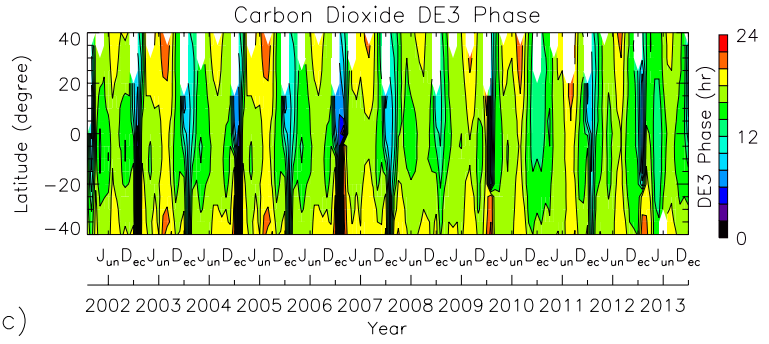
Carbon Dioxide DE3 Phase
Latitude (degree)
40
20
0
−20
−40
DE3 Phase (hr)
24
12
0
Jun Dec Jun Dec
2002 2003 2004 2005 2006 2007 2008 2009 2010 2011 2012 2013
Year

c)

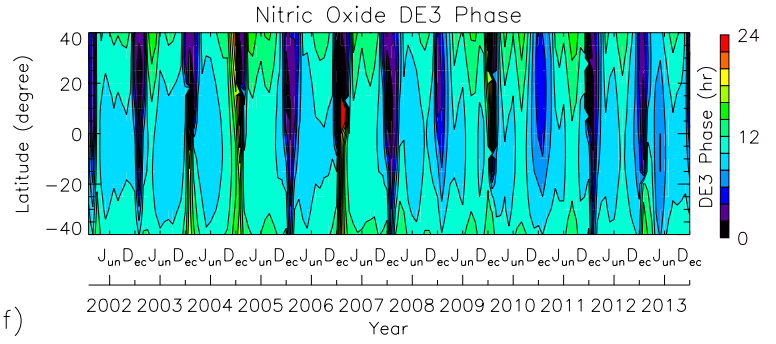
Nitric Oxide DE3 Phase
Latitude (degree)
40
20
0
−20
−40
DE3 Phase (hr)
24
12
0
Jun Dec Jun Dec
2002 2003 2004 2005 2006 2007 2008 2009 2010 2011 2012 2013
Year

f)

Figure 9.

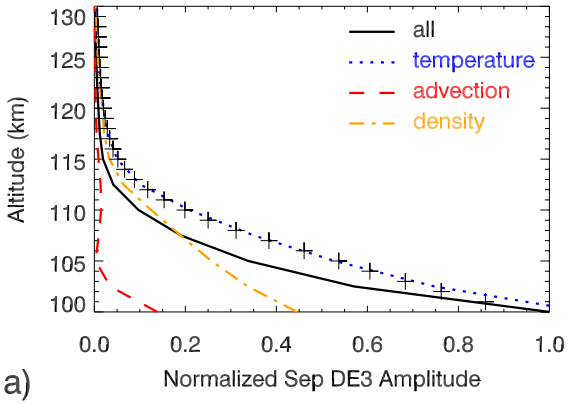
all
temperature
advection
density
Altitude (km)
130
125
120
115
110
105
100
0.0
0.2
0.4
0.6
0.8
1.0
Normalized Sep DE3 Amplitude

a)

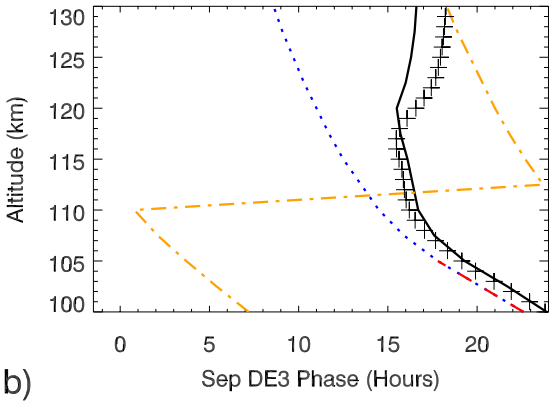
Altitude (km)
130
125
120
115
110
105
100
0
5
10
15
20
Sep DE3 Phase (Hours)

b)

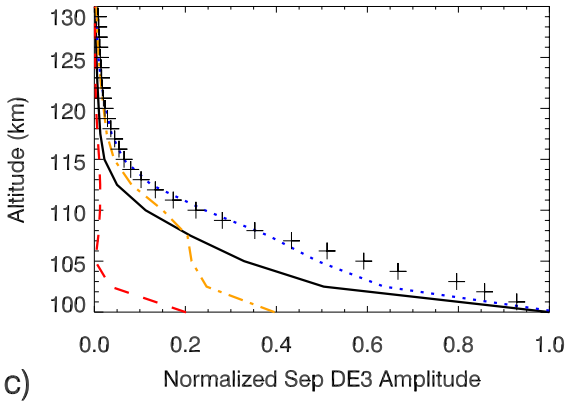
Altitude (km)
130
125
120
115
110
105
100
0.0
0.2
0.4
0.6
0.8
1.0
Normalized Sep DE3 Amplitude

c)

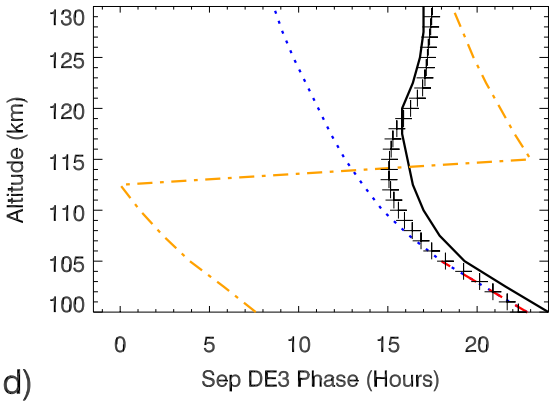
Altitude (km)
130
125
120
115
110
105
100
0
5
10
15
20
Sep DE3 Phase (Hours)

d)

Figure 10.

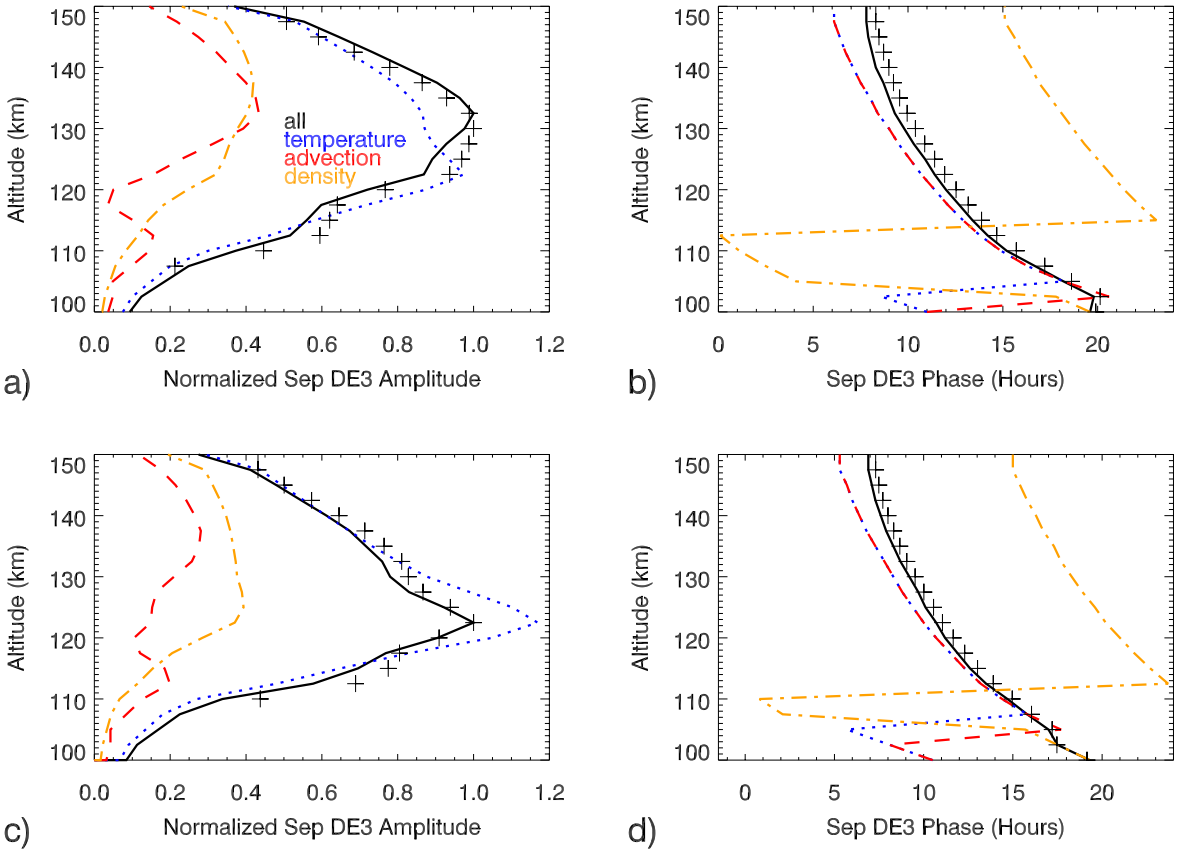
Altitude (km)
150
140
130
120
110
100
0.0
0.2
0.4
0.6
0.8
1.0
1.2
Normalized Sep DE3 Amplitude
all
temperature
advection
density
a)
0
5
10
15
20
Sep DE3 Phase (Hours)
b)
c)
d)

Figure 11.

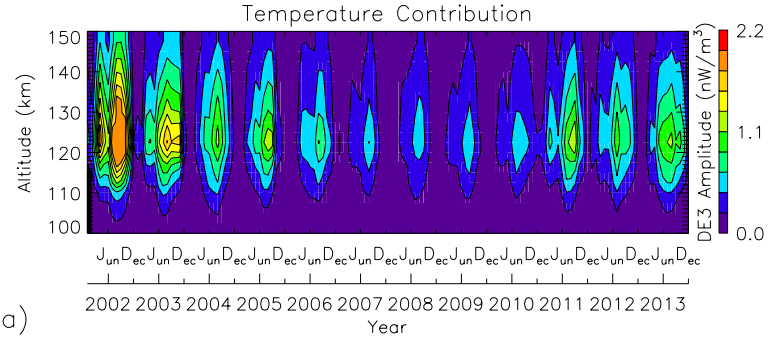
Temperature Contribution
Altitude (km)
150
140
130
120
110
100
DE3 Amplitude (nW/m³)
2.2
1.1
0.0
Jun Dec Jun Dec
2002 2003 2004 2005 2006 2007 2008 2009 2010 2011 2012 2013
Year

a)

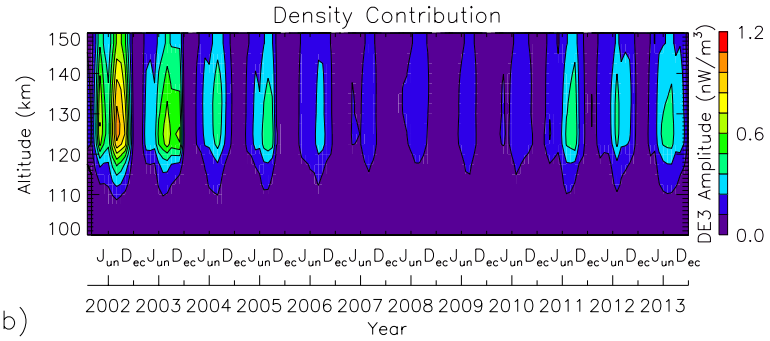
Density Contribution
Altitude (km)
150
140
130
120
110
100
DE3 Amplitude (nW/m³)
1.2
0.6
0.0
Jun Dec Jun Dec
2002 2003 2004 2005 2006 2007 2008 2009 2010 2011 2012 2013
Year

b)

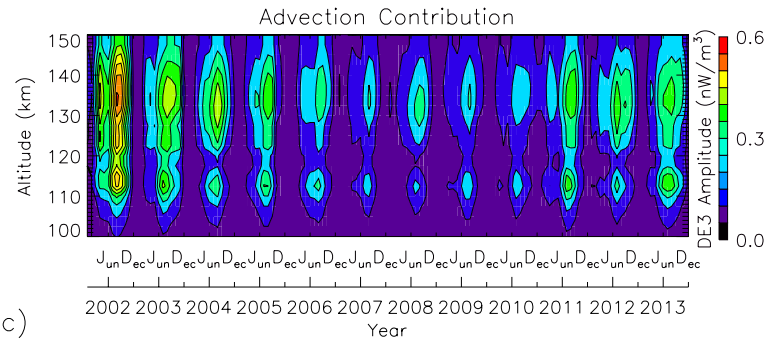
Advection Contribution
Altitude (km)
150
140
130
120
110
100
DE3 Amplitude (nW/m³)
0.6
0.3
0.0
Jun Dec Jun Dec
2002 2003 2004 2005 2006 2007 2008 2009 2010 2011 2012 2013
Year

c)

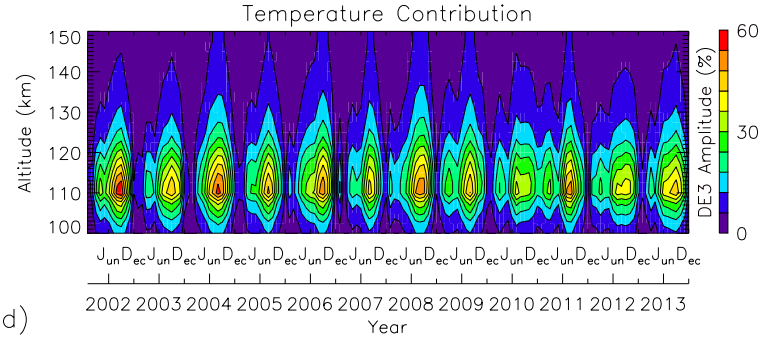
Temperature Contribution
Altitude (km)
150
140
130
120
110
100
DE3 Amplitude (%)
60
30
0
Jun Dec Jun Dec
2002 2003 2004 2005 2006 2007 2008 2009 2010 2011 2012 2013
Year

d)

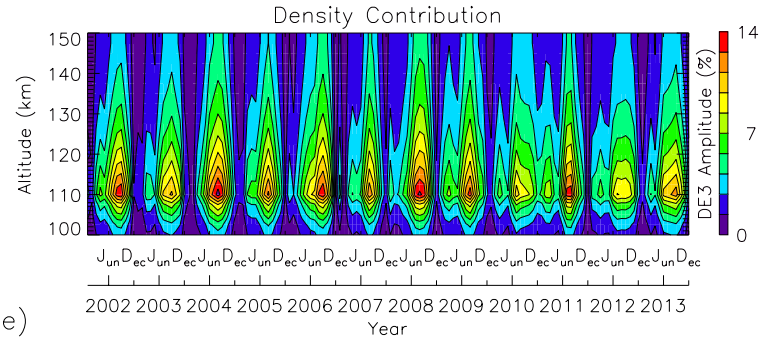
Density Contribution
Altitude (km)
150
140
130
120
110
100
DE3 Amplitude (%)
14
7
0
Jun Dec Jun Dec
2002 2003 2004 2005 2006 2007 2008 2009 2010 2011 2012 2013
Year

e)

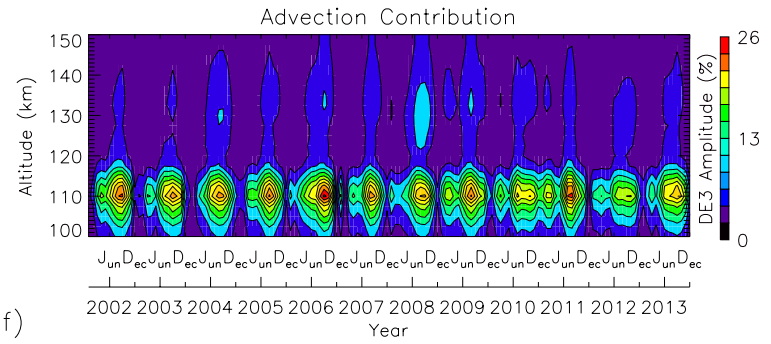
Advection Contribution
Altitude (km)
150
140
130
120
110
100
DE3 Amplitude (%)
26
13
0
Jun Dec Jun Dec
2002 2003 2004 2005 2006 2007 2008 2009 2010 2011 2012 2013
Year

f)

Figure 12.

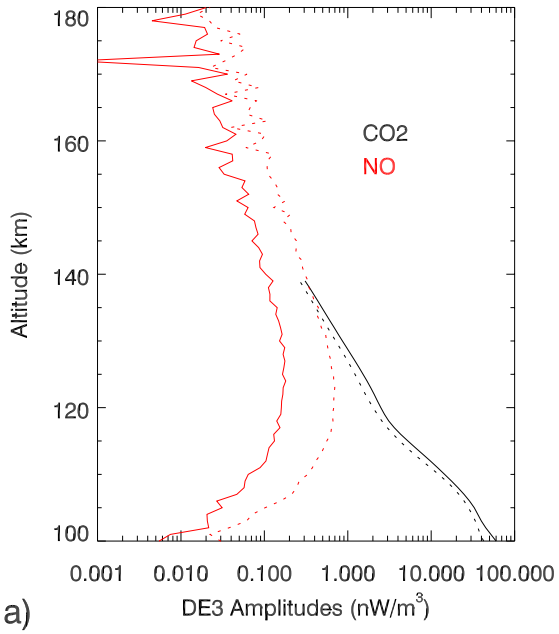
180
160
140
120
100
Altitude (km)
CO2
NO
0.001
0.010
0.100
1.000
10.000
100.000
DE3 Amplitudes (nW/m3)

a)

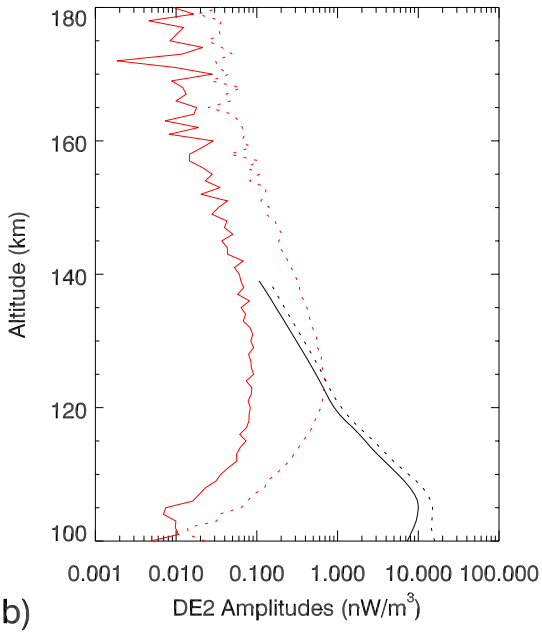
180
160
140
120
100
Altitude (km)
0.001
0.010
0.100
1.000
10.000
100.000
DE2 Amplitudes (nW/m3)

b)